

Radio Frequency Interference from Radio Navigation Satellite Systems: simulations and comparison to MeerKAT single-dish data

Brandon N. Engelbrecht,^{1*} Mario G. Santos,^{1,2} José Fonseca,^{3,4,1} Yichao Li,^{5,1}
 Jingying Wang,^{6,1} Melis O. Irfan,^{7,1} Stuart E. Harper,⁸ Keith Grainge,⁸ Philip Bull,^{8,1}
 Isabella P. Carucci,^{9,10} Steven Cunnington,⁸ Alkistis Pourtsidou,^{11,12,1} Marta Spinelli,^{13,1}
 Laura Wolz⁸

¹*Department of Physics & Astronomy, University of the Western Cape, Cape Town 7535, South Africa*

²*South African Radio Astronomy Observatory (SARAO), 2 Fir Street, Cape Town, 7925, South Africa*

³*Instituto de Astrofísica e Ciências do Espaço, Universidade do Porto CAUP, 4150-762 Porto, Portugal*

⁴*Departamento de Física e Astronomia, Faculdade de Ciências, Universidade do Porto, Rua do Campo Alegre 687, PT4169-007 Porto, Portugal*

⁵*Department of Physics, College of Sciences, Northeastern University, Wenhua Road, Shenyang, 11089, China*

⁶*Shanghai Astronomical Observatory, Chinese Academy of Sciences, 80 Nandan Road, Shanghai, 200030, China*

⁷*Institute of Astronomy, Madingley Road, Cambridge CB3 0HA, UK*

⁸*Jodrell Bank Centre for Astrophysics, Department of Physics and Astronomy, The University of Manchester, Manchester M13 9PL, UK*

⁹*INAF - Osservatorio Astronomico di Trieste, Via G.B. Tiepolo 11, 34131 Trieste, Italy*

¹⁰*IFPU - Institute for Fundamental Physics of the Universe, Via Beirut 2, 34151 Trieste, Italy*

¹¹*Institute for Astronomy, The University of Edinburgh, Royal Observatory, Edinburgh EH9 3HJ, UK*

¹²*Higgs Centre for Theoretical Physics, School of Physics and Astronomy, The University of Edinburgh, Edinburgh EH9 3FD, UK*

¹³*Observatoire de la Côte d'Azur Laboratoire Lagrange, Bd de l'Observatoire, CS 34229, 06304 Nice cedex 4, France*

Accepted XXX. Received YYY; in original form ZZZ

ABSTRACT

Radio Frequency Interference (RFI) is emitted from various sources, terrestrial or orbital, and create a nuisance for ground-based 21cm experiments. In particular, single-dish 21cm intensity mapping experiments will be highly susceptible to contamination from these sources due to its wide primary beam and sensitivity. This work aims to simulate the contamination effects emitted from orbital sources in the Radio Navigational Satellite System within the 1100-1350 MHz frequency. This simulation can be split into two parts: (I) satellite positioning, emission power, and beam response on the telescope and (II) fitting of the satellite signal to data in order to improve the original model. We use previously observed single dish MeerKAT L-band data which needs to be specially calibrated to include data contaminated by satellite-based RFI. We find that due to non-linearity effects, it becomes non-trivial to fit the satellite power. However, when masking regions where this non-linearity is problematic, we can recreate the satellite contamination with high accuracy around its peak frequencies. The simulation can predict satellite movements and signal for past and future observations, which can help in RFI avoidance and testing novel cleaning methods. The predicted signal from simulations sits below the noise in the target cosmology window for the L-band (970 - 1015 MHz) making it difficult to confirm any out-of-band emission from satellites. However, a power spectrum analysis shows that such signal can still contaminate the 21cm power spectrum at these frequencies. In our simulations, this contamination overwhelms the auto-power spectrum but still allows for a clean detection of the signal in cross-correlations with mild foreground cleaning. Whether such contamination does exist one will require further characterization of the satellite signals far away from their peak frequencies.

Key words: satellites – 21cm intensity mapping – RFI

1 INTRODUCTION

The integrated emission of the 21cm line of neutral hydrogen (HI) can be used to map the Large Scale Structure (LSS) of the Universe.

* E-mail: engelbrechtbn@gmail.com

The method, known as intensity mapping (IM), allows us to scan large areas of the sky without the need to resolve individual galaxies (Bharadwaj et al. 2001; Chang et al. 2008; Chang et al. 2010; Masui et al. 2013; Bull et al. 2015). Detecting this faint cosmological signal can be hindered by radio frequency interference (RFI) emitters which, due to the technological evolution of communication devices (Bentum et al. 2010), have been increasingly contaminating the radio bands. These sources consist of terrestrial RFI, such as frequency modulation (FM) broadcasting towers, and orbital RFI, which emanates from the satellites (Baan 2010). The main techniques applied to mitigate the effects of RFI have been: avoidance, filtering, and flagging (Baan 2019). Radio telescopes are planned and operate within a designated radio quiet region, which aids in restricting contamination. However, as much as we locate radio facilities away from terrestrial RFI, satellites in orbit around the Earth will always contaminate the signal and become one of its largest contaminants. This is of particular worry as satellites transmitting in the L-band frequency range between 1 and 2 GHz, contaminating regions of the spectrum important for HI IM. The situation will only worsen due to the increasing number of satellites being launched annually (ITU 2021). Real-time filtering schemes can prevent the leakage of strong RFI signals into the frequencies of interest before correlation (Buch et al. 2023, e.g.). The usual approach, however, is to flag (e.g. remove) post-correlation data contaminated by RFI (Offringa et al. 2012).

As radio telescopes grow more sensitive and the sky becomes more contaminated with satellites, it becomes crucial to fully understand the radio signal emitted by them. Such a study serves three purposes: 1) to find parts of the sky and times when observations are less contaminated; 2) to understand how much the RFI contaminates the target frequencies for our science; and 3) to test if there are ways to further clean the signal from RFI on those target frequencies (away from the prominent peaks). There are several examples of follow-ups on satellite emissions and their impact on observations. The Green Bank Telescope (GBT)¹ has been characterizing the sources of RFI at different frequency bands. The Five Hundred Metre Telescope (FAST)² has looked at estimating the power of various satellites by using an extra antenna to monitor nearby satellites (Wang et al. 2021a). The Parkes³ ultra-wide bandwidth receiver (Hobbs et al. 2020) contained navigational and telecommunication satellites within their observation. A detailed study of the MeerKAT RFI environment as a function of direction, frequency, time of day and baseline has also been done⁴.

Satellite emissions can be particularly adverse for single-dish HI IM surveys such as those planned for BINGO (Battye et al. 2013) and FAST (Bigot-Sazy et al. 2016) as well as the MeerKAT (Santos et al. 2017) and SKAO-MID (Santos et al. 2015) arrays when used as a collection of single dishes. Although interferometers are also affected, the signal is further reduced due to time and frequency smearing (decorrelation) away from the delay centre. The more direct mitigation strategy is to consider frequencies far away from the allocated satellite transmission band. These allocations are set by the International Telecommunications Union (ITU), but there is still out-of-band transmission since the ITU only provides guidelines for

the maximum out-of-band power that can leak out of these allocations (ITU 2004, 2015). Given that the HI cosmological signal is less than a mK, one needs to understand how satellite RFI propagates outside the allocated bands, and gauge if their contamination is negligible.

With the cosmological surveys planned for MeerKAT and the Square Kilometre Array Observatory (SKAO), it is becoming increasingly important to study the impact of this emission at the SKAO site in South Africa. The situation should be better for surveys using MeerKAT's UHF band (580 - 1015 MHz) and SKAO-MID band 1 (350 - 1050 MHz), but it will be more problematic for MeerKAT's L-band (900 - 1670 MHz) and SKAO-MID band 2 (950 - 1760 MHz). Harper & Dickinson (2018) estimated the impact of global navigational satellite systems (GNSS) on a future SKAO-MID band 2 HI IM survey, using models for the total power and spectral structure of GNSS signals convolved with a model SKA beam. They conclude that for frequencies > 950 MHz, the emission from GNSS satellites will exceed the expected HI signal for all angular scales. However, information is quite sparse on the technical specifications of satellites, namely the signal's amplitude which introduces uncertainties in the modelling. Moreover, the impact on the final HI IM power spectrum depends on the scanning strategy used. Also, one could use cleaning methods to reduce the contamination level, or even subtract it as in Finlay et al. (2023).

In this work, we will expand the analysis in Harper & Dickinson (2018) (referred to as HD18 hereafter) using a complete catalog that incorporates radio navigational satellite systems (RNSS) extending beyond the focus of GNSS to include regional and augmented systems. We develop new simulations that are compared and fitted to calibrated MeerKAT data from Wang et al. (2021b) ("W21" from now on). This data was used to make a recent detection of the cross-correlation power spectrum between HI and galaxy surveys (Cunnington et al. 2023a). We focus on satellites with allocated emission bands below 2 GHz, which should have the largest impact on the target cosmology window (970 - 1015 MHz). In total, we consider 73 satellites operating in MeerKAT's field-of-view during the scanning period of an observation commencing on 25-02-2019 02:40:11 SAST⁵. The new set of simulations can accurately estimate satellite contamination over a wide frequency range once properly calibrated with the data. In this work we will determine in which regimes we can calibrate and characterise the satellite signals. Additionally, we will use this simulation to understand the impact of satellites on the HI IM 3d power spectrum and test cleaning methods. These results will help in preparing observations with future surveys with MeerKAT and the SKAO and set the stage to understand the ultimate level of contamination on the science that will be extracted from such data.

The remainder of the paper is organized as follows: in section 2, we describe how we construct the navigational satellite signals and positions; in section 3, we address the calibration of the observational data to include the previously flagged RFI region; in section 4 we discuss the effectiveness of the model; in section 5 we explore the applications of the model; and conclude in section 6.

2 NAVIGATIONAL SATELLITE SYSTEMS SIMULATION

Artificial satellites address a host of objectives, ranging from communication, earth observation photography, navigational informa-

¹ <https://greenbankobservatory.org/rfi-scans-and-known-sources/>

² <https://fast.bao.ac.cn/>

³ <https://www.parkes.atnf.csiro.au/>

⁴ <https://skaafrika.atlassian.net/wiki/spaces/ESDKB/pages/305332225/Radio+Frequency+Interference+RFI>

⁵ South African Standard Time

tion, and so on. In this paper, we focus only on radio navigational satellite systems, including sub-categories such as global, regional, and augmented systems. The different systems within these sub-categories are usually referred to as constellations. These constellations cater to and have slight differences between civilian and military uses for a given country. Currently, there are four global navigational satellite systems in orbit which provide positional information to users across the globe. These are the United States of America - NAVSTAR, referred to as *GPS*, the European - Galileo system, which we will refer to as *GAL*, the Russian - Global'naya Navigatsionnaya Sputnikovaya Sistema (GLONASS), which we will refer to as *GLO*, and the Chinese Compass navigation system Beidou, which we will refer to as *BEI*.

On the other hand, Regional navigational systems operate across a specific country or fixed geography. Here we will consider the Indian Regional Navigation Satellite System NavIC, referred to as *IRNSS* and the Japanese Quasi-Zenith Satellite System, referred to as *QZS*. Another system incorporated into this work is the Satellite Based Augmentation System (SBAS). This geostationary satellite system benefits the current GNSS by improving positioning accuracy. These constellations follow operational standards, such as allocated frequency bands, which follow the ITU recommendations (ITU 2004, 2015).

In Table B2, we list the navigational satellite systems considered in this work. This catalog contains information on the aforementioned constellations, including the relevant parameters required to model their spectral signal emission (see following subsections). We have used several sources in the literature to collect this information. However some details are unavailable or quite uncertain, such as the satellite signal's transmitted power in some constellations. This has prompted us to allow some of these parameters to be free and later fitted to the data as explained in subsection 2.4.

In order to build a simulation of the observed satellite signal, the following information is needed:

- The frequency range of the observation $\Delta\nu_j$ [MHz];
- The timestamps t [sec] of the observation;
- Location of the telescope on the Earth [Lat & Long.];
- Observational pointing per timestamp [RA & Dec];
- an all-sky telescope beam model;
- positional information of the satellites
- the power emitted by the satellites as a function of frequency.

The location information, telescope pointing, and beam model are flexible and can be user-specific, allowing the simulation to be applied to various single-dish radio telescope experiments around the globe. The following subsections explain in more detail the steps taken to simulate the observed satellite signal.

2.1 Satellite position

Each navigational constellation/system comprises several individual satellites. These individual satellites follow a predetermined course at a specific orbital distance. Although celestial mechanics could naively predict the position of the satellites, there are several effects that make this difficult to calculate over long time scales and up to date information is required. The positional vector information for each satellite is contained within a two-line element (TLE) dataset on the Celestrak⁶ database. The data is saved as snapshots for the various satellite constellations. This catalogue is updated every

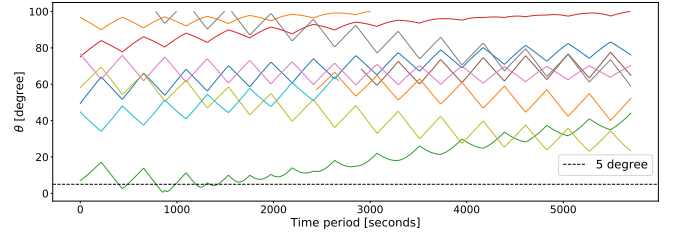


Figure 1. The angular distance to the telescope pointing direction (Equation 1) for various satellites in the GALILEO constellation (solid lines represent). The black dashed line represents an angular distance of 5°.

24 hours and does not store previous TLE information. Historical TLE information from months to years back can be accessed via the Wayback Machine⁷. The Wayback Machine stores snapshot from various days but not concurrently. However, when comparing historical and present snapshots, we have found that a TLE can reliably describe a satellite position within 3 months. Therefore, when selecting historical snapshots, we simply use the one closest to the observation dates.

Once the necessary TLE information has been acquired, we apply the python package `Skyfield`⁸ (Rhodes 2019) to load the TLE vectors and retrieve the orbital positions of the individual satellite, such as latitude & longitude; right ascension (RA) & declination (DEC) or azimuth & altitude (elevation) for a reference position on Earth. In our case, we took the position to be the central location of the MeerKAT array: Longitude: 21° 26' 38" E and Latitude: 30° 42' 47.41" S. Given that the diameter of the MeerKAT array is much smaller than the orbital height of the navigational satellites, each antenna will observe the satellites at approximately the same angular distance to the beam centre.

The final ingredient is the angular distance, θ , between the satellite and the pointing direction of the telescope, which can be calculated through (Duffett-Smith & Zwart 2017):

$$\cos(\theta) = \sin(al_p) \sin(al_s) + \cos(al_p) \cos(al_s) \cos(az_p - az_s) \quad (1)$$

where az/al is the azimuth/altitude and the subscripts p/s represent the telescope pointing and satellite position respectively. The telescope pointing can be provided from a scanning strategy or taken directly from the observation data files. The satellite position and telescope pointing are calculated for every time stamp in the scan (2-second resolution in this work).

In Figure 1, we show the angular distances of various satellites within the GAL constellation for one of the observational scans taken from actual MeerKAT data. The seesaw structure is related to the fast scanning strategy adopted for this observation. Individual satellites can move below the telescope horizon and are then ignored. The appearance or disappearance of satellite information within the observation window illustrates this. We see that a single satellite from the GAL constellation passes directly through the pointing centre of the telescope.

2.2 Beam response

To effectively simulate the observed signal of the satellites present in the data, we require an accurate description of the MeerKAT

⁶ www.celestrak.com

⁷ <https://archive.org/web/>

⁸ <https://rhodesmill.org/skyfield/>

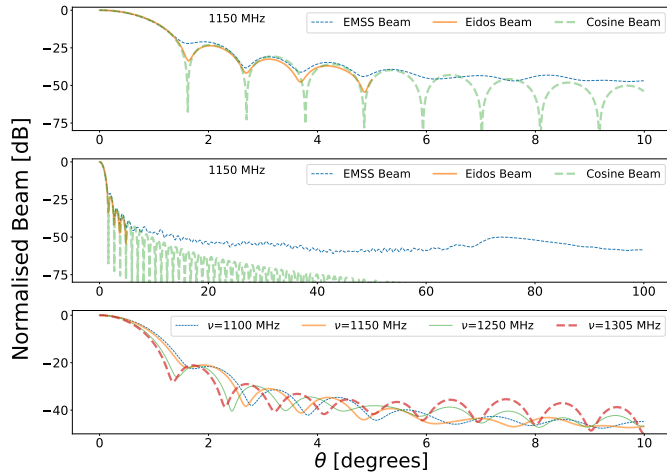


Figure 2. The different beam models available in the simulation. In the 1st & 2nd panels we show the beam models: EMSS (blue thin dashed), Eidos (orange solid) and Cosine (green thick dashed) at 1150 MHz, with the 2nd panel up to higher angular separation (θ). The 3rd panel shows the EMSS beam at different frequencies: 1100 MHz (blue thin dashed), 1150 MHz (orange thick solid), 1250 MHz (thin green solid), and 1305 MHz (red thick dashed).

beam response. An accurate beam model will inform us not only of the main lobe of the telescope but, more importantly, of the side lobe structure as well as its frequency dependence. In [Asad et al. \(2021\)](#), the MeerKAT beam model was measured and fitted to a radius of 5° . However, satellite emission beyond this radius can still affect our observations ([Harper & Dickinson 2018](#)). Therefore we decided to use a MeerKAT L-band beam model based on detailed electromagnetic simulations provided by the company EMSS Antennas⁹, which offers the response of the MeerKAT antenna in the horizontal HH and vertical VV polarizations. These simulations cover a frequency range of 900-1670MHz and an angular range of $0^\circ - 100^\circ$. Above that, we set the beam response to zero.

Note that we only consider the spherically averaged beam, so there is only dependence on the angular distance from the beam centre (the polar angle, " θ "). In reality, beams are asymmetrical. The MeerKAT beam was measured to deviate from this symmetry at less than 1% within the main lobe, although the deviation can become much larger at the second sidelobe and above (see [Asad et al. 2021](#); [de Villiers 2023](#)). The provided EM simulations have an angular resolution of 0.1° and a frequency resolution of 2 MHz, so interpolation was done both in angle and frequency. The code also provides the holographic beam model from [Asad et al. \(2021\)](#), which we refer to as "Eidos", and the analytical "Cosine beam" which is a reasonable fit to the MeerKAT beam ([Mauch et al. 2020](#)). The top and middle panel of [Figure 2](#) shows a comparison between these models. We see that above 10° the Cosine model starts deviating from the simulation.

In this paper, we only consider total intensity measurements. Although satellite emission can be polarised, modelling that is difficult and so we combine both polarisations both in the simulation and in the observed data (usually called horizontal, HH, and vertical VV, polarisations). The beam model is also normalised to be one at its maximum. The bottom panel of [Figure 2](#) highlights the EMSS

beam model as a function of the angular separation for different frequencies.

2.3 Power-Spectrum Density

The power spectrum density (PSD) is the spectral response of the transmitted signal by the satellite. The signal along frequency can be described as a combination of sine and cosine waves, which we refer to as the modulation of the signal. The simplest of these modulations is a constant pulse known as binary phase shift keying (BPSK), which, when Fourier transformed, is described by:

$$P_{\text{BPSK}(n_c)}(\nu) = \frac{\text{sinc}(\pi(\nu - \nu_c)/[n_c f_0])}{\sqrt{n_c f_0}}, \quad (2)$$

where $f_0=1.023$ MHz is the reference frequency, n_c is the chip rate, which refers to the rate at which a phase change occurs, and ν_c is the central frequency of the signal.

The signal's PSD is then given by the auto-correlation ([Teunissen & Montenbruck 2017a](#)):

$$S_{xx}(\nu) = |P_{xx}(\nu)|^2, \quad (3)$$

where xx is the modulation type and $S_{xx}(\nu)$ is normalised to integrate to 1 over frequency. In [Figure 3](#) we show other, more complex signal modulation types used in the simulation (see appendix A). Currently, our model can simulate binary-phase shift keying (BPSK); binary offset carrier (BOC); alternative BOC (alt-BOC), multiplexed BOC (MBOC) and time-MBOC (TMBOC). We list all the modulations used in this paper and the variables needed for them in table B2. These signals will be present at all frequencies, although the out-of-band emission will be smaller. It is possible that there is extra dampening of the signal away from the main peak but such information is not available and so we assume these modulations are a good representation of the signal at all frequencies. Estimating if the level of out-of-band emission is correct is one of the goals of this paper and will be addressed in a later section.

2.4 Signal temperature

Each satellite can emit a combination of different signals with specific modulations as described in the previous section. For each of these signals, i , the observed brightness temperature from one satellite is calculated as:

$$T_{\text{sat}, i}(t, \nu) = B(\theta, \nu) S_{xx_i}(\nu) \frac{P_i}{r^2} \frac{c^2}{4\pi\nu^2 k_b}, \quad (4)$$

where ν is the observed frequency, k_b is the Boltzmann constant and c the speed of light in the vacuum. The beam response is given by $B(\theta, \nu)$, where again, $\theta(t)$ represents the angular separation between the satellite position and the pointing centre of the telescope and is a function of time. The radial distance between satellites and the telescope on Earth $r(t)$ is also a function of time and is calculated with the *Skyfield* package ([Rhodes 2019](#)). Because the channel width for MeerKAT is very small, we neglect variations in S_{xx} and just take the value at the central frequency of the channel, ν .

P_i represents the total emitting power for the signal i , which is defined using the transmitter antenna gain G_{t_i} (dBi) and the transmitted power P_{t_i} (dBW):

$$P_i = \frac{G_{t_i} P_{t_i}}{4\pi}. \quad (5)$$

The spectral energy distribution, SED (units of power per frequency) for each signal from a satellite is given by the product of P_i and

⁹ <https://www.emssantennas.com/>

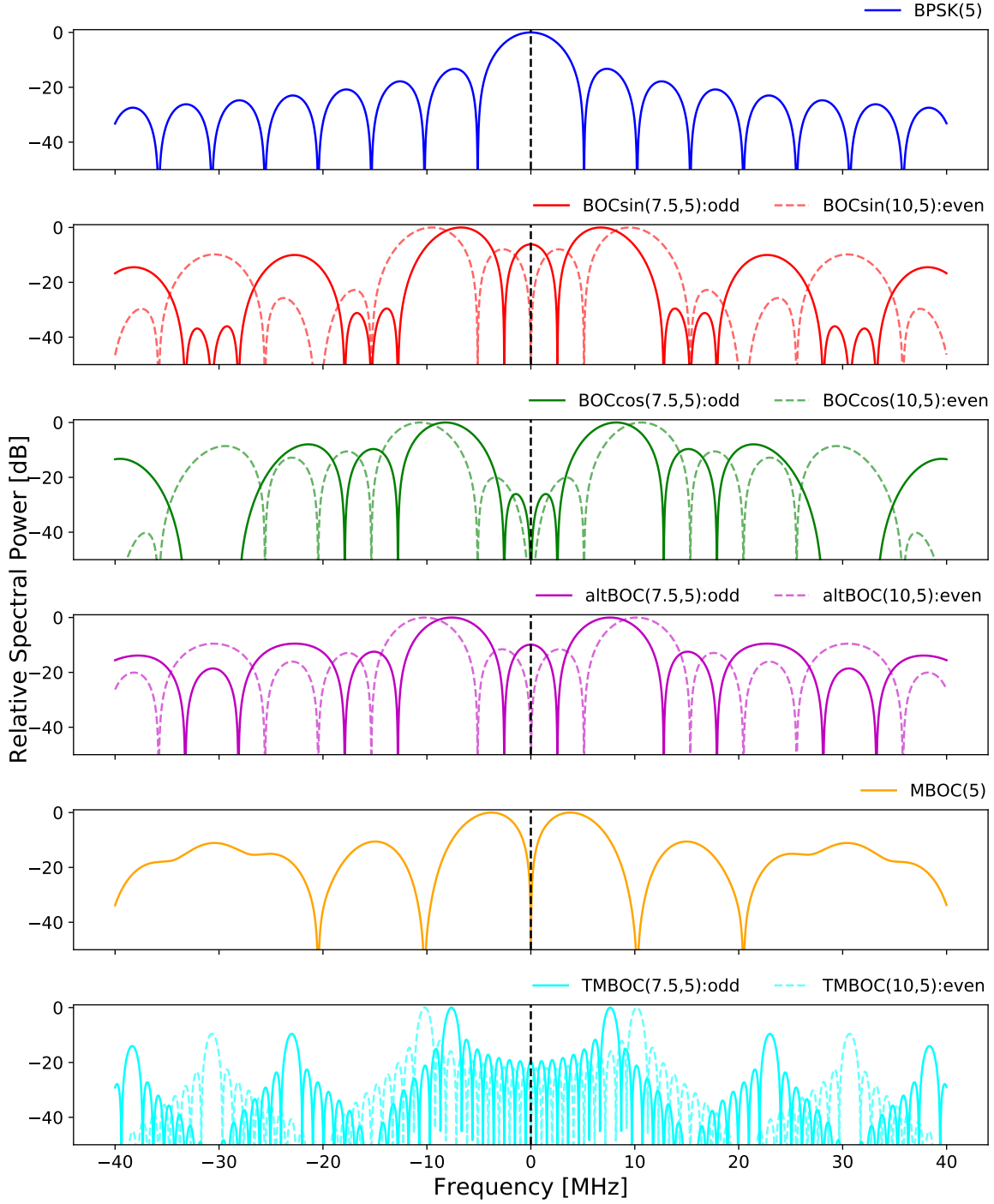


Figure 3. Normalised Power Spectrum Density of transmission patterns. Solid lines represent odd values of n and dashed lines even ones. Starting from the top panel : BPSK; sine BOC; cosine BOC; altBOC; MBOC and TMBOC. In [Table B2](#), we highlight the various modulation types employed by the GNSS.

S_{xx_i} . In some instances, the signal power values are not known to the public, and therefore, we selected a value of $P_t = 10$ dBW and $G_t = 10$ dBi where required.

Note that we neglect the satellite beam in the modeling, e.g. we assume the satellite is always pointing towards the telescope. This beam is supposed to be quite wide and so any directional effect should be negligible, specially for satellites not far away from the telescope zenith. The situation will be more uncertain for satellites

far away from the telescope position as they will be pointing down, not towards the telescope.

The values used for each signal can be found in [Table B2](#). The first column corresponds to the index i used to identify the signal. Not all signals in the table are used in our simulation because their peak emission is quite far from our target frequency band and their contribution should be negligible compared to the others.

For simplicity, we will assume that every satellite of a given

Observation ID	Antenna no.	Date/Time (UCT)
1551055211	m000	2019-02-25 00:40:11
1553966342	m000	2019-03-30 17:19:02
1554156377	m000	2019-04-01 22:06:17
1556138397	m000	2019-04-24 20:39:57
1562857793	m004	2019-07-11 15:09:53

Table 1. The 5 observational blocks used in the analysis. The block ID, antenna number and date and time of the observation are listed. The results, unless stated otherwise, are shown for the highlighted observation.

constellation emits all the signals listed for that constellation (highlighted in grey in Table B2). This might not be necessarily true, as we know that of the listed signals some belong to specific generations of a constellation. As an example younger satellites could have additional signals on board compared to their predecessors. However, such information is again not publicly available in most circumstances. So, in the simulation, we sum over all satellite signals for a given constellation and constellations as described in the beginning of section 4. The terms $B(\theta, \nu)$ and r are then calculated for each satellite individually. Note again that if the satellite is below the horizon at the telescope site or is more than 100° away from the pointing centre we remove it from the calculation.

3 OBSERVED SATELLITE SIGNAL

To build and test our GNSS satellite simulation, we used the MeerKAT observational data described in W21. This data is a single-dish HI IM pilot survey that mapped a region of around 200 deg^2 centred at $ra \sim 11\text{h}$ and $dec \sim 0^\circ$ over the L-band, which ranges between $\approx 980\text{--}1700 \text{ MHz}$ over a span of 4096 channels and a frequency resolution of 0.2 MHz (see Figure 4). The observations are split into blocks of about 1.5h, each covering the same area with all dishes pointing in the same direction. The data is taken in both linear polarisations, horizontal (HH) and vertical (VV). A standard single-dish flux/bandpass calibrator is observed before and after each block, and noise diodes are fired every 20 seconds in order to calibrate gain fluctuations in time. The observation blocks used in this analysis are listed in Table 1. In the next sections, we show the results for block 1551055211, dish m000 only, unless stated otherwise.

In Figure 5, we show different frequency regions contaminated by RFI for one of the blocks. The light-grey shaded region (920–960 MHz) corresponds to the Global System for Mobiles (GSM), aeroplane transponders, etc. (Sihlangu et al. 2020). The dark grey shaded region at higher frequencies (1520–1630 MHz) corresponds to telecommunication services and a few navigational satellites. The region shaded in green corresponds to our frequencies of interest (1140–1310 MHz) which navigational satellites’ RFI dominates. As a reference, our target cosmology window used to make a cross-correlation detection of the power spectrum with the same data (Cunnington et al. 2023a) is at 973–1015 MHz. As mentioned before, we ignore the navigational satellites present in the high L-band frequency range since their contribution should be subdominant at 1140–1310 MHz compared to the satellites emitting there (and even less in the target cosmology band).

3.1 Calibration of the RFI-contaminated region

In principle, one would like to use the gain solutions derived in W21. From that, we could calibrate the TOD (time-ordered data)

for each block, dish and polarisation using:

$$T_{\text{cal}}(t, \nu) = T_{\text{raw}}(t, \nu)/g(t, \nu), \quad (6)$$

where T_{cal} is the calibrated temperature in Kelvin, $T_{\text{raw}}(t, \nu)$ the raw visibility in correlator units, and $g(t, \nu)$ is the gain. Unfortunately, the calibration pipeline used in W21 immediately flagged the 1100–1350 MHz region for all times due to the strong RFI. This poses a problem for us since we need the data to be calibrated in that frequency interval in order to compare to our simulations. In Figure 6, we show the derived gain from W21 for one block and one dish and the HH and VV polarisations (top and bottom, respectively). Left panels show the gain as a function of time, averaged over frequency and right panels the time average as a function of frequency (only non flagged times and frequencies are included in these averages).

Using a point source to calibrate the flagged region is quite challenging due to the very strong RFI signal. Noise diodes could be better, but their frequency dependence is not very well known from the lab and again, calibrating the noise diodes beforehand with a point source would have the same contamination issues in the target RFI contaminated region. Instead, we took a different approach. We first assume that the gain can be broken into the temporal (g_t) and frequency (g_ν) components, e.g. $g(t, \nu) \approx g_t(t)g_\nu(\nu)$. This basically means that the bandpass shape is assumed constant throughout the observation, with only an overall amplitude variation in time. Such assumption is well supported by the analysis in W21, with frequency-dependent variations measured to be less than 1%. The gain can then be written as

$$\tilde{g}(t, \nu) = \frac{\langle g(t, \nu) \rangle_\nu \langle g(t, \nu) \rangle_t}{\langle g(t, \nu) \rangle_{t, \nu}}, \quad (7)$$

where \tilde{g} is used to represent the new derived gain. The averages, $\langle \rangle$, are over the non flagged times and frequencies. This immediately gives us the time variation of the gain as in Figure 6.

Obtaining g_ν is more complicated due to the missing information. A simple solution would be to interpolate the frequency curve in Figure 6, but the gap is too wide. To obtain more points for the interpolation, we assumed that the frequency dependence of the gain follows the frequency dependence of the raw visibilities without the satellites. This implies that the input temperature should be flat across the frequency gap, except for the satellites. In reality, the ground pickup, receiver temperature and galactic synchrotron have a slope. However, this effect will be small in the interval considered and can be corrected later when matching to the gain solution outside the RFI band. Below we describe in detail the steps we followed to complete the missing frequency information in the gain maps:

- We start from the raw visibility of both HH & VV polarizations before RFI flagging. We then select the minimum visibility values across time for each frequency channel, which we take as an estimate of the floor level of the channel when satellites are not present. We do this in the frequency range spanning 1000–1500 MHz, which is wider than the RFI-contaminated band, but it allows us to obtain the tail-end information for the frequency area we wish to calibrate;
- The next step is to remove all the peaks in the data caused by the satellite contamination, to get a smooth curve of the floor level. We start by doing a spline fit to this minimum raw visibility which provides a smooth curve in frequency. We then take the difference between the spline and minimum raw visibility curves. From the

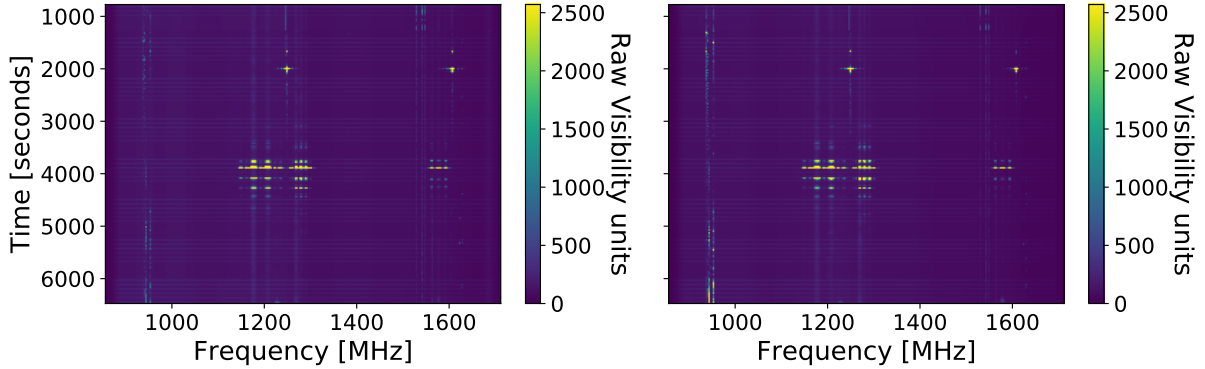


Figure 4. Raw visibility maps of antenna m000 for HH (right) and VV (left) polarizations for the observation scanning period as a function of frequency and time. The bright spots correspond to saturation in the receiver due to strong RFI, such as when satellites pass close to the pointing (see Figure 1).

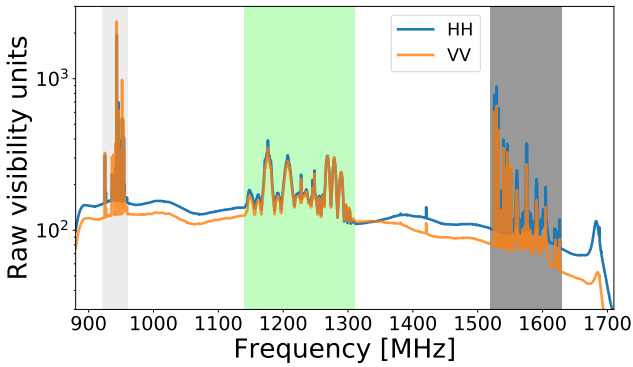


Figure 5. The time-average of Figure 4, with the HH (blue curve) and VV (orange curve) polarizations shown for the m000 antenna. The light-grey (920-960 MHz) shaded region represents the low-end RFI, which stems from Global System for Mobiles (GSM) and aeroplane transponders (Sihlangu et al. 2020). The green-shaded region (1140-1310 MHz) represents our frequency range of interest dominated by the navigational satellite RFI. The dark grey (1520-1630 MHz) shaded region relates to the higher frequency RFI in the L-band, which contains signals from a few navigational services but is dominated by telecommunication services.

residual, a sigma clip¹⁰ is then applied to remove the peaks that stem from the satellite emission. We then interactively applied this procedure to the clipped curve until no more clipping was needed (after five interactions). We then obtained a smooth overlay spanning the affected frequency channels as seen in Figure 7;

- The resulting smooth curve represents the underlying base’s structure of the raw visibility and we assume that the gain will be proportional to this. We then normalize the smooth curve by matching it to the known gain from W21 outside the satellite’s frequency region. We did this between 1138MHz and 1307MHz for the HH polarization and between 1100MHz and 1314MHz for the VV polarization. Finally, we create a smooth function (spline) that becomes the final frequency component of the gain map, as seen in Figure 8.

The final temperature map from the data will be the average of the calibrated temperatures, $T_{\text{cal}}(t, \nu)$, from each polarisation.

¹⁰ https://docs.astropy.org/en/stable/api/astropy.stats.sigma_clip.html

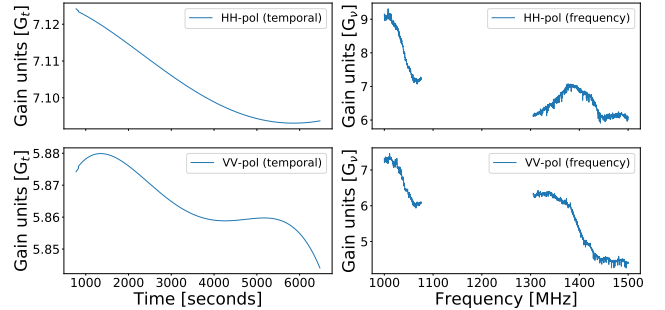


Figure 6. Functional form of the gain as a function of time (left panels) and frequency (right panels) for m000 antenna (Wang et al. 2021b). The top panels are for HH polarization and the bottom ones for VV. RFI flagging results in the missing information in frequency.

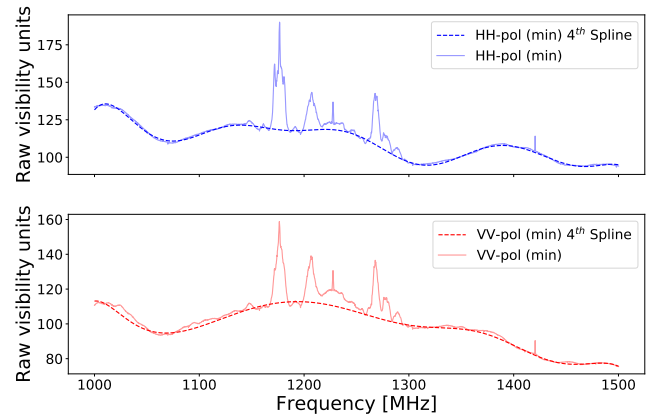


Figure 7. Estimate of the base raw visibility without satellites after the 4th iterative clipping (dashed line) overlaid on antenna m000 minimum raw visibility (solid line) for the HH (top) and VV (bottom) polarizations.

3.2 Background model

In order to compare the satellite simulation to the data, we also need to factor in the other temperature contributions, which we call the background model. This background is much smaller than the satellite emission and reasonably flat in frequency, making up the baseline level we see in Figure 5. We follow W21 to model this

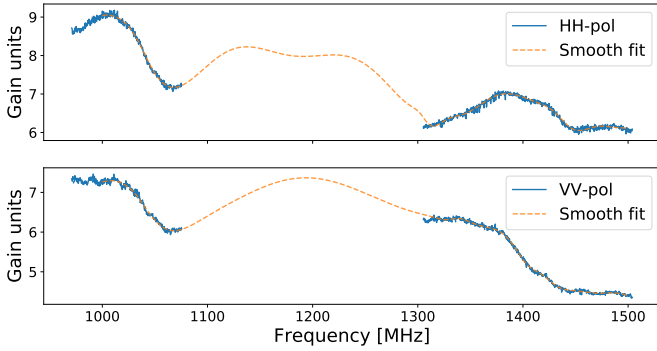


Figure 8. The bandpass of the gain for the m000 antenna in the HH (top panel) and VV (bottom panel) polarization. The blue curve represents the available gain information from W21; the orange dashed curve represents the best estimate of the gain across the frequency region of interest.

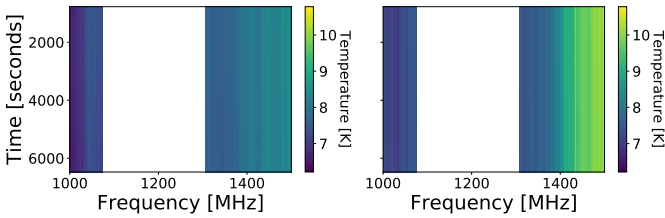


Figure 9. Receiver temperature for the m000 antenna in HH (left panel) and VV (right panel) polarization. RFI cleaning results in missing channel frequency information from 1075 to 1305 MHz

background temperature (T_{BG}) as

$$T_{BG}(t, \nu) = T_{rec}(t, \nu) + T_{el}(t, \nu) + T_{gal}(t, \nu) + T_{CMB}, \quad (8)$$

where T_{rec} is the receiver temperature, T_{el} depends on the elevation and includes contributions from the ground spill and atmosphere, T_{gal} is the synchrotron emission from the Galaxy and T_{CMB} is Cosmic Microwave Background (CMB) temperature.

T_{CMB} is constant, and since the observations were done at constant elevation, T_{el} should be constant in time. The same is expected from T_{rec} since the instrument is quite stable over the course of the 1.5h observation. T_{gal} will change as the telescope pointing moves through the sky but these fluctuations will be at ~ 0.1 K level. So we could in principle just remove most of this background contribution by subtracting a constant in time. We would then have to do the same to the satellite simulation for a proper comparison. This would mean we wouldn't be able to fit for the satellites DC level which can be useful for other situations. So in this paper, we didn't remove any time offset and instead included T_{BG} in the simulation. For this, we use the same models as in W21. However, since the receiver temperature was calculated as part of the calibration process in W21, the frequencies corresponding to satellite emission are also flagged (Figure 9).

To restore the masked information, we will follow the same approach as the one used to estimate the gain in the RFI-contaminated band. We assume that the receiver temperature is a separable function in time and frequency, which is then proportional to the frequency and time average of $T_{rec}(t, \nu)$, respectively. These averages do not use any of the flagged data, and this is done for each block, dish and polarization. Again, the function in time is already continuous. For the frequency dependence, we interpolate the known data points (solid blue in Figure 10) using a radial basis function

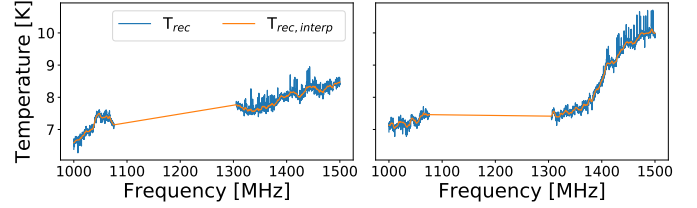


Figure 10. A time-averaged representation of the receiver temperature along frequency for the m000 antenna with HH (left) and VV (right) polarization. The blue curve is the receiver temperature from the model, whilst the orange dash curve is the RBF interpolation overlaid. In the lower and higher frequencies, the RBF follows the data and makes the best attempt to connect the high and low-frequency values.

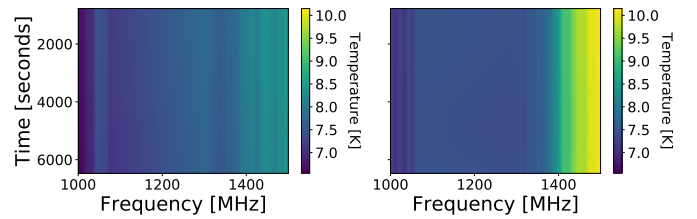


Figure 11. Interpolated receiver temperature for the m000 antenna in the HH (left panel) and VV (right panel) polarization.

(RBF¹¹). This results in a curve (orange line) covering the whole frequency range (Figure 10). In this instance, we do not have any data points in the RFI-flagged region, which makes the interpolation more uncertain. However, looking at the fluctuations in Figure 10, one should expect any deviations to be less than 0.5 K. Since this is an additive quantity to the far stronger satellite signal, such errors should have little impact in the analysis. We plot the final receiver temperature used in Figure 11.

4 FITTING THE SATELLITE SIMULATION TO OBSERVATIONS

In this section, we aim to determine how well the simulation performs in recreating the navigational satellite signals we see in the observational data of the MeerKAT telescope. We compare the simulated satellite signal $T_{sat}(t, \nu)$ to the calibrated observations from each block. In this regard, we have to combine the background model of subsection 3.2 to that of $T_{sat}(t, \nu)$. This allows us to obtain the same temperature base component between the observation and simulation. Our results, which are centred around 1100-1350 MHz, extend toward the tail of the spectrum, where the background model dominates.

The signal modelling presents a few uncertainties, namely, in the overall amplitude of the temperature of a signal from a constellation. The emitting power and gain of the satellite are not constant with time, and we expect it to be reduced as the satellite ages. Moreover, in some cases, the values tabulated in the literature appear as upper limits or are not available. Uncertainties in the telescope primary beam or calibration errors can also affect the results. Because of these issues, we introduce a set of α_i parameters associated with

¹¹ <https://docs.scipy.org/doc/scipy/reference/generated/scipy.interpolate.Rbf.html>

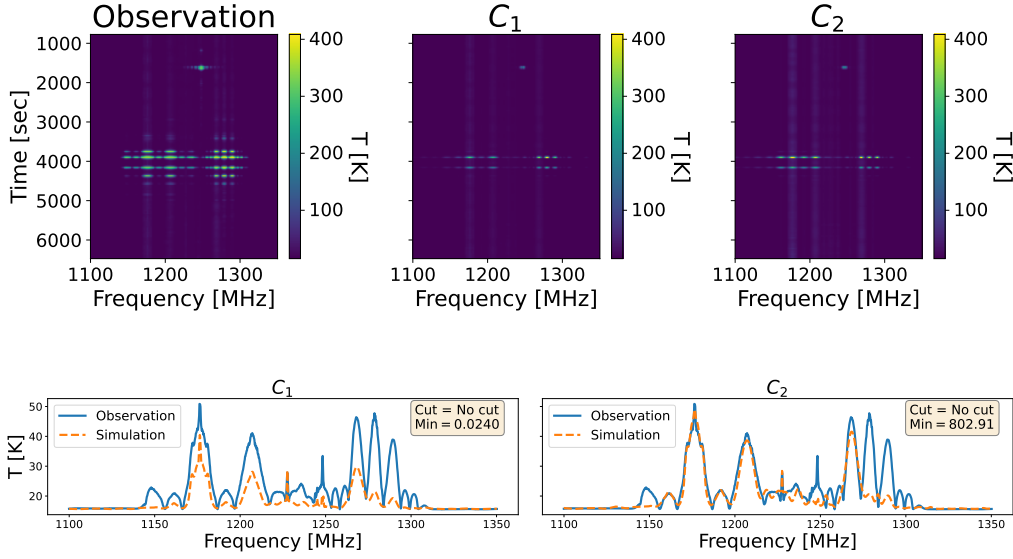


Figure 12. Best-fit comparison for the *no-mask scenario*. The 1st row shows the waterfall images for the observation (left) and the simulation: case 1 (centre) and case 2 (right). The temperature colour bar was set at the maximum and minimum values corresponding to the observation. The 2nd row shows the time-averaged frequency plane of the waterfall plots, with the left panel being the C_1 case and the right being the C_2 case. The solid blue curve represents the observation, and the dashed orange curve represents the simulation’s best fit for the two cases.

the overall amplitudes of each signal within a given constellation:

$$T_{S,i}(t, \nu) = \alpha_{\text{sat}, i} T_{\text{sat}, i}(t, \nu), \quad (9)$$

where $T_{S,i}$ is the simulated temperature of the i -th signal and $T_{\text{sat}, i}$ is given by Equation 4. Each signal in Table B2 has an associated $\alpha_{\text{sat}, i}$. This amplitude is assumed constant in frequency and time, although we do fit it to different time ranges in the sections below. Note that if there is a good match between the model and the observations, these α s should equal one. The number of parameters introduced depends on the number of relevant signals that fall within our frequency range of interest and which constellations are visible to the telescope. The total simulated signal is then:

$$T_S(t, \nu) = \sum_{\text{constellation}} \sum_{ij} \alpha_{\text{sat}, i} T_{\text{sat}, i}^j(t, \nu) + T_{\text{BG}}(t, \nu), \quad (10)$$

where we sum over all constellations, i runs over the signals present in each constellation and j runs over the satellites in that constellation.

4.1 Fitting the α_i amplitudes

In order to fit for the α_i , we minimize a cost function (CF) which we define as

$$\text{CF} = \frac{1}{N} \sum \frac{(T_O - T_S)^2}{\sigma_D^2}, \quad (11)$$

where T_O is the adjusted calibrated observational data and T_S is the simulated temperature response. N is the total number of points used in the fit and is used just for normalisation when we compare cases with different number of data points. The sum is over all times and frequencies of the time-ordered data. σ_D^2 can be seen as a weight

for each data point, and we consider two distinct cases:

$$\sigma_D = \begin{cases} T_O \text{ [case 1 (} C_1 \text{)]} \\ \text{or} \\ 1 \text{ [case 2 (} C_2 \text{)]} \end{cases}$$

Case 1, denoted as C_1 below, uses the temperature itself, which is proportional to the expected thermal noise as in the radiometer equation. Essentially, this would correspond to the standard χ^2 . This can also be seen as minimizing the percentage difference between the model and the data. The problem with this cost function is that the uncertainties in the model should dominate the expected thermal noise, since at 2 seconds and 0.2 MHz resolution, the thermal noise gives an error of about 0.1% for each data point. This case basically down-weights the data in the region where the satellite’s signal is the brightest so that the fitting will be dominated by the (many) small temperature values in the region where the background model dominates, making it harder to fit the rather important bright satellite peaks. For this reason, we also consider case 2 (denoted as C_2 below), where all the data points are equally weighted, i.e., $\sigma_D = 1$.

The minimisation of the cost function is accomplished with the `scipy.optimize.minimize` package¹² using the *Powell* method. The initial conditions for the α parameters are set to zero for the first iteration; a lower bound of zero and an unconstrained upper bound are placed on the parameters as boundary conditions. A tolerance threshold (tol) of 1e-6 is applied to the minimisation as a convergence limit. If a signal is never used in a given observation (because the corresponding satellites are too far away from the pointing direction) then the α will stay at zero.

The results of the fitting to block 1551055211 are shown in Figure 12. We see that although some of the main features are fitted, the amplitude of the simulation signal is smaller and misses some

¹² <https://docs.scipy.org/doc/scipy/reference/generated/scipy.optimize.minimize.html>

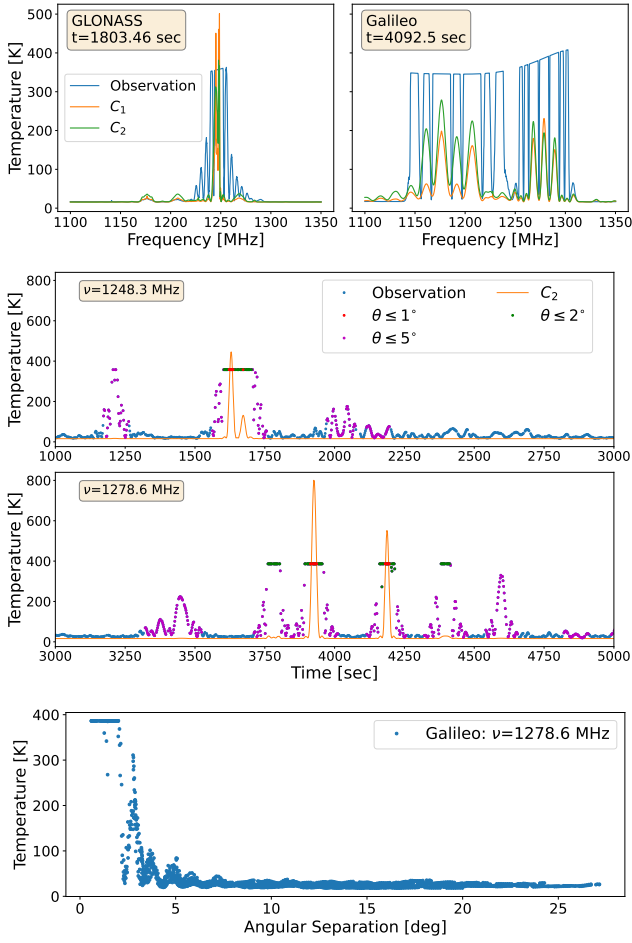


Figure 13. A snapshot of the data along different axes: frequency (1st panel), time (2nd & 3rd panels) and along the angular separation of a Galileo satellite: GSAT0209-(PRN-E09) (4th panel). In the 1st panel, the data (blue), C_1 case (orange), and C_2 case (green) at two different timestamps correspond to incursions from the GLONASS (left panel) and Galileo (right panel) constellations. The snapshot is when $\theta \leq 1^\circ$ for both constellations; it also reveals the peak frequency of GLONASS at ~ 1248 MHz. However, in the case of the Galileo constellation, the peak is hidden due to the saturation of the receiver. In the 2nd & 3rd panels, based on the information in the 1st panel, we select the peak frequencies from Table B2. The 2nd panel is at 1248.3 MHz (GLONASS), and the 3rd panel at 1278.6 MHz (Galileo). The observational data are shown with blue dots, the C_2 case is shown in orange, and the limits of incursion by the satellites are shown for the 1° , 2° , 5° in red, green and magenta respectively. In the 4th panel, we show the observed temperature versus the angular separation values for the Galileo satellites at the frequency selected around which the satellite operates.

of the peaks. This is better seen in the bottom panel, where we take a time average of the waterfall plot. This is true for both cost functions, although case 2 performs better. The solid blue represents the observational data, while the dashed orange line represents the simulation best-fit results for the C_1 (left) and C_2 (right) cases, with a minimum value of the cost function of 0.0240 and 802.91 respectively. The reason for this is that the observation saturates when the satellites get too close to the telescope, which makes our model break down. In this block, two satellites passed through the telescope’s pointing. The first belongs to the GLONASS constellation and breached the $\theta \leq 1^\circ$ between 1622.39-1672.37 seconds. While the second satellite belongs to the Galileo constellation (see

Figure 1), and was within the $\theta \leq 1^\circ$ between 3913.426-4195.30 seconds. This saturation is not clear in the bottom panel of Figure 12 because we averaged over time and only a small percentage of the time is saturated. This is better seen in Figure 13. The top panel shows the signal across frequency for the snapshot at the time when the signal is stronger (satellites close to the pointing). Note that the saturation/cut-off level is not constant across frequency. The two middle panels show the total signal along time for the peak frequencies belonging to the GLONASS constellation (left panel) at 1248.3 MHz, and the Galileo constellation (right panel) at 1278.75 MHz. Although other signals (and satellites) may contribute to these frequencies, these are the dominant ones. The fluctuations in time should depend on the angular distance to the pointing direction and follow the primary beam shape. The solid orange line represents the simulation best-fit results for the C_2 case only while the dots represent the observational data, with different colors corresponding to different angular distances. Below 2° the telescope system completely saturates at these frequencies.

The bottom panel of Figure 13 shows the calibrated temperature from the observed block at the frequency of 1278.6 MHz against the expected movement of the Galileo satellite GSAT0209-(PRN-0E09)¹³. The position is calculated exactly for the observation date and timestamps and the angular distance is derived with respect to the dish pointing centre, taking into account the movement of the dishes as well. Although other signals will “contaminate” this frequency, we can clearly see the shape of the MeerKAT primary beam as expected. Besides contamination from other satellites (at other angular distances) there are other reasons why the comparison to the primary beam isn’t perfect, in particular the saturation of the signal and small errors in the satellite position. These errors have a greater impact as the satellite approaches the dish pointing. Finally we note that the saturation not only imposes a cutoff on the observed signal but also makes the gain non-linear. This non-linearity can affect most frequencies when the signal becomes strong, even outside the peak frequency, and can show up even before saturation. However our model was built assuming the telescope response was linear even in the presence of navigation satellite RFI. As we can see, this is not always true and will affect our fit to the data. Thus, this poses the question of addressing the saturation issue by masking pixels/time stamps where the telescope response becomes non-linear. I.e., can we improve the model that recreates the satellite’s emissions? We will explore these possibilities in the following section.

4.2 Testing limits of validity

From now on we will only consider the C_2 case to test the limits of validity of our approach. In all masking scenarios we have compared C_1 with C_2 and concluded that C_2 gives better overall fits.

4.2.1 Angular Masking

In order to address the saturation/non-linearity of the data which affects the fitting, we start by trying to remove any points that correspond to satellites close to the observation direction. Using a simulation with the same observation specifications, we calculate the positions of all the satellites as in Figure 1 and remove timestamps corresponding to an angular distance below a certain threshold. This

¹³ <https://www.euspa.europa.eu/european-space/galileo/programme>

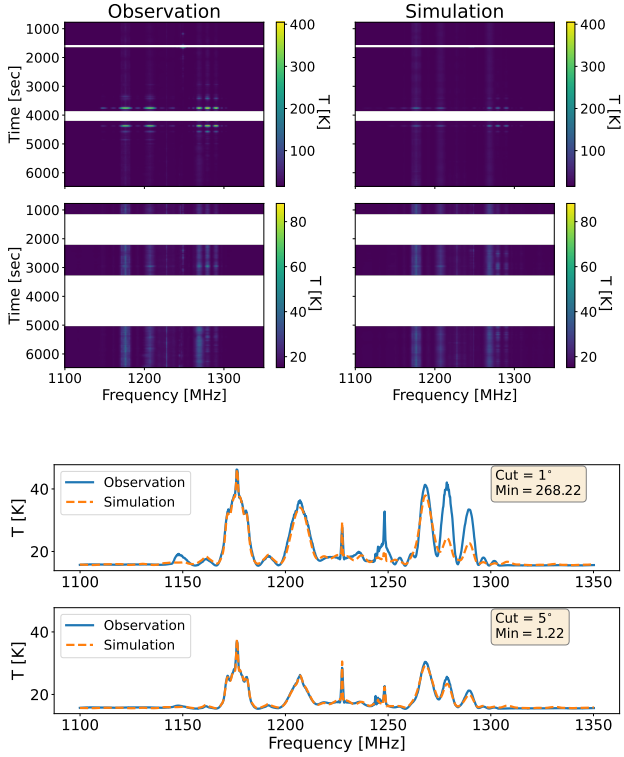


Figure 14. The best-fit comparison for the *angular masking scenario*. The waterfall images (1st & 2nd row) for the various angular are displayed: the observation (left) and the simulation (right). The 1st row shows the 1°, and the 2nd row shows the 5° angular masking cut, respectively. In the 3rd & 4th row are the time averaged results as a function of frequency for the two angular cuts. The observation is in solid blue curve and the simulation in dashed orange.

is done on both the observation data and simulations. We used an angular cut of 1° and 5°. The results can be seen in Figure 14. A satellite with $\theta \leq 1^\circ$ would be found inside the main lobe of the MeerKAT beam and saturate the signal, while $\theta \leq 5^\circ$ should also remove the contribution of satellites that can cause non-linearity effects on the receivers without necessarily saturating the signal. We can see that indeed the fitting performs much better for the cut with 5°. On the other hand, the 5° cut means that any satellite with a weaker signal will probably be below the error and won't be fitted for. Moreover, this cut is quite aggressive, removing up to 48% of the data while the 1° will remove about 6%. Note that these implications for the fit refer to the main peaks in the data. The effect at lower frequencies where we do our cosmological analysis is very hard to see and doesn't impact the fit.

4.2.2 Thermal Masking

This approach tries to address the issue of saturation directly, by making cuts when the temperature goes above a certain threshold. This is applied to the observation data both across time and frequency and the mask is then transferred to the simulation. The threshold values for the thermal cut are 25 K, 50 K, and 100 K, corresponding to 19%, 2% and 1% of data loss respectively. The results are shown in Figure 15. The fitting improves as more of the saturated pixels are removed. However, this is still not as good as the

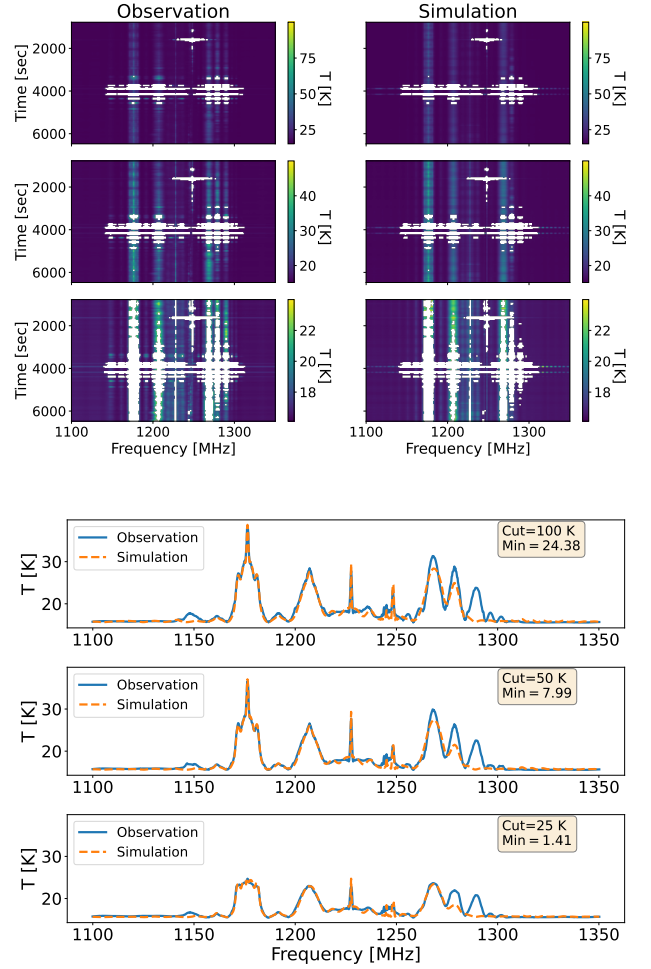


Figure 15. The best-fit comparison for the *thermal masking scenario*. The waterfall images (1st, 2nd & 3rd rows) with the observation (left), and the simulation (right). The time-averaged results below in the 4th, 5th & 6th rows, with the observation (solid blue curve) and simulation (dashed orange curve). The various thermal thresholds given are: 100 K (1st row), 50 K (2nd row), and 25 K (3rd row).

5° scenario, even for the 25K cut, as can be seen by the frequency plots or the minimum values of the cost function. This is more obvious for the emission above 1250 MHz, which is a contribution from the Galileo E6 and Beidou B1-2 & B3 signals. Also, on the lower end of the frequency scale, around 1150 MHz, the simulation does not fit for the smaller peaks, in particular the second side lobe emanating from the central peak at ~1175MHz. It is also interesting to note that the thermal cut of 25K limits the peak contributions from satellite signals, removing more signal there than the 5° cut.

4.2.3 Full Thermal Masking

In the previous scenario, only the "pixels" in time and frequency that exceeded a given threshold were flagged. We now consider a case where all the points across frequency are flagged for a given time as long as one of the values exceeds that cut-off. The reasoning is that once the receiver system saturates, the gain will become non-linear, affecting all frequencies, not just those where the signal hits the limit. Since the saturation limit seems to change between blocks,

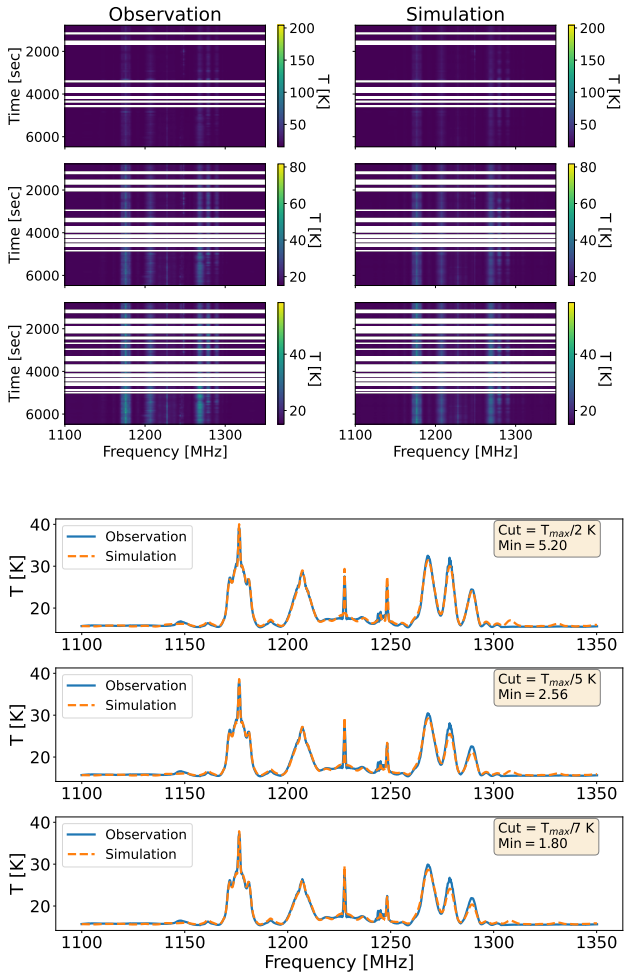


Figure 16. The best-fit comparison for the *full thermal masking scenario*. The waterfall images (1st, 2nd & 3rd rows) with the observational (left), and the simulation (right). The time-averaged results below in the 4th, 5th & 6th rows, with the observation (solid blue curve) and simulation (dashed orange curve). The various pixel thermal limit are set at: 50.00% (1st & 4th row), 20.00% (2nd & 5th row), and 14.29% (3rd & 6th row) of the maximum temperature.

we decided to use a percentage of the maximum pixel value from each block instead of the threshold. We applied masking thresholds of : $T_{\max}/2$, $T_{\max}/5$, and $T_{\max}/7$ and show the results in Figure 16. For this block (ending 211) and antenna m000, the maximum temperature T_{\max} is ≈ 400 K, which correlates to temperature thresholds of ≈ 200 K, ≈ 80 K and ≈ 60 K respectively. As seen from the time average plots in the bottom panels, the fits are quite good, even for the higher-level thresholds. In particular, they are clearly better than the equivalent temperature cut in the previous scenario. This shows that there is indeed unmodeled contamination away from the peak frequencies, probably due to non-linearities, which is removed by flagging the full-time dump. At the same time, the level of data loss is smaller than, say, the 5°, with 7%, 14% and 20% for each threshold.

Table 2 summarises the results from the different fitting approaches. There is a clear trend of improvement as we remove more of the strong peaks, which should remove the saturated data points in the system. Other things could contribute to this improvement,

Masking Type	C_2	% flagged data
Angular		
1°	261.24	5.4
5°	1.21	47.55
Thermal		
100 K	24.47	1.39
50 K	7.99	2.25
25 K	1.41	9.23
Full Thermal		
$T_{\max}/2$	5.20	7.49
$T_{\max}/5$	2.56	14.25
$T_{\max}/7$	1.80	20.1

Table 2. The minimum cost function (C_2) values for various masking scenarios and the % of data that is flagged per scenario.

such as reducing the out-of-band signal which is hard to model. In the next sections, we discuss possible issues in our model that could affect this fitting besides the expected saturation/non-linearity.

4.2.4 Time variation of the α parameters

The α parameters are used to renormalise the satellite total power amplitude. In that sense, they should have little to no time evolution since the satellite signal should be stable in time. Three situations can change this. First, uncertainties in the telescope’s primary beam, such as asymmetries, could be absorbed into the α s, which can then change depending on the position of the satellite with respect to the telescope pointing. Second, as the observed signal is always a mix of different satellites, it won’t be a surprise if different values of the same α s provide a better fit depending on what satellites appear in the field of view. But such variations should be small when one single signal dominates the data. A third reason for time evolution (and difficulties in the fitting) is that individual satellites from a given constellation might not be emitting the exact same signals as we assume. The α amplitudes will try to correct for this and might change as these satellites from the same constellation go in and out of the field of view.

In Figure 17, we show the observation and fitting for three different time windows, corresponding to 775-1000 seconds, 2200-2400 seconds and 5500-6200 seconds. These time periods were picked so that no satellites enter the 5° zone to avoid saturation/non-linearities. Figure 18 shows the fitted α parameters. We can see a non-negligible variation in some of the α s. In particular, $i = 5, 7, 9, 12, 14$, which is probably due to satellites from Galileo and GLONASS entering the field of view. We note again that since the starting values for the α s before the fit are set to zero, an α moving from zero just means that the satellites with the corresponding signal have moved into the field of view. However, once an α becomes non-zero, it should keep that value, if not for the abovementioned reasons.

A better way to see the fitting accuracy is through the residuals as in Figure 19. A reason for the observed difference could be that the frequency shapes used in the modelling (taken from literature, see Table B2) do not accurately follow the real satellite signal. When taking the time average of the residuals, the narrow spikes around ≈ 1225 MHz show the width of the peak is not captured perfectly in the model; this peak is associated with the GPS-L2 signal. Similarly, peaks at 1246 MHz & 1248 MHz, belonging to Glonass-L2 signals, are not accurately accounted for by the simulation throughout the different time periods that are seen in the observational data. Another example is the dip at 1305 MHz, indicating that the model

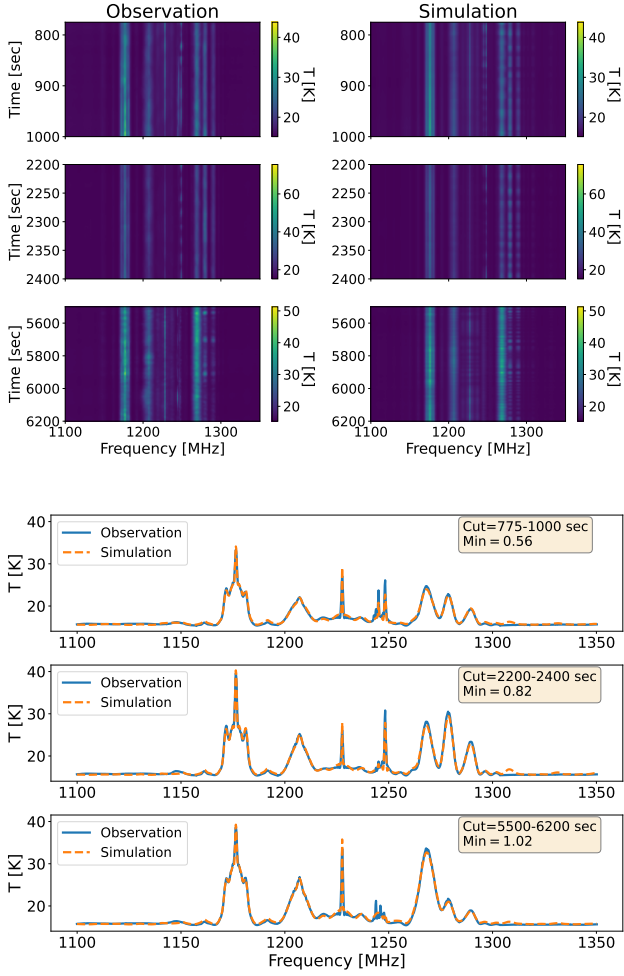


Figure 17. The best-fit comparison for different time windows. The waterfall images (1st, 2nd & 3rd rows) with the observation (left), and the C_2 case (right). The time-averaged results below in the 4th, 5th & 6th rows, with the observation (solid blue curve) and simulation (dashed orange curve). The various temporal periods are set at 775-1000 sec (1st & 4th row), 2200-2400 sec (2nd & 5th row), and 5500-6200 sec (3rd & 6th row).

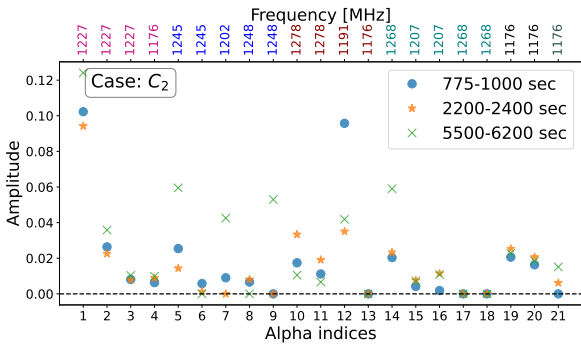


Figure 18. The α amplitudes fitted to each temporal window (Figure 17). The different periods are 775-1000 (blue ●), 2200-2400 (orange ★) and 5500-6200 (green ×). The central frequency of each α signal is shown on the top y-axis. For the constellations: GPS-violet ($\alpha_1 - \alpha_4$), Glonass-blue ($\alpha_5 - \alpha_9$), Galileo-dark red ($\alpha_{10} - \alpha_{13}$), Beidou-teal ($\alpha_{14} - \alpha_{18}$), IRNSS-black ($\alpha_{19} - \alpha_{20}$) and SBAS-dark grey (α_{21}).

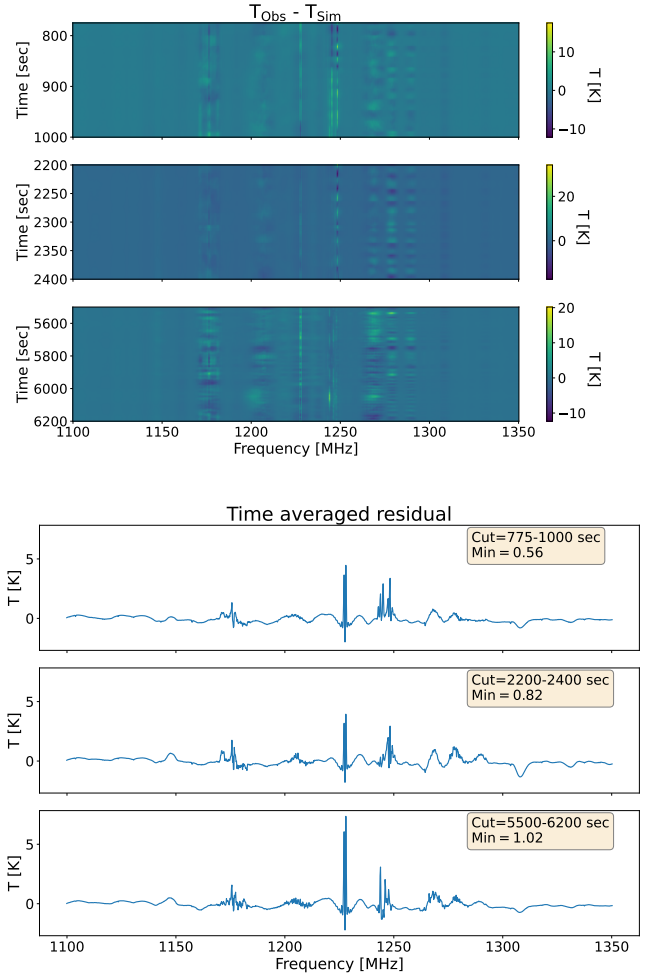


Figure 19. The residual 2d and time-averaged residual 1d for the *temporal masking scenario* (Figure 17). The various temporal periods are set at 775-1000 sec (1st & 4th row), 2200-2400 sec (2nd & 5th row), and 5500-6200 sec (3rd & 6th row).

has a peak that is not seen within the observational data; a possible explanation is that the out-of-band transmissions are being dampened; such dampening is not accounted for in our current modeling of the satellite signals.

4.2.5 Positional errors

One last issue we will check with the fitting is the possibility of positional errors. As the dishes move back and forth, an error in the satellite position will translate to an amplitude difference that changes with time. To test this, we isolate the movement of one GAL satellite that gets very close to the telescope pointing and focus on 1278.75 MHz, corresponding to one of the peak frequency emissions from the GAL constellations. The immediate neighbouring channels to the peak frequency are averaged to increase the signal-to-noise.

For this test, we use the data from above with temporal windows that do not have any satellites below 5° . Including data below the 5° cutoff would make the result more obvious, but it would be affected by saturation and non-linearities. In Figure 20, we show the signal ratio between the observation and the simulation. As the dishes

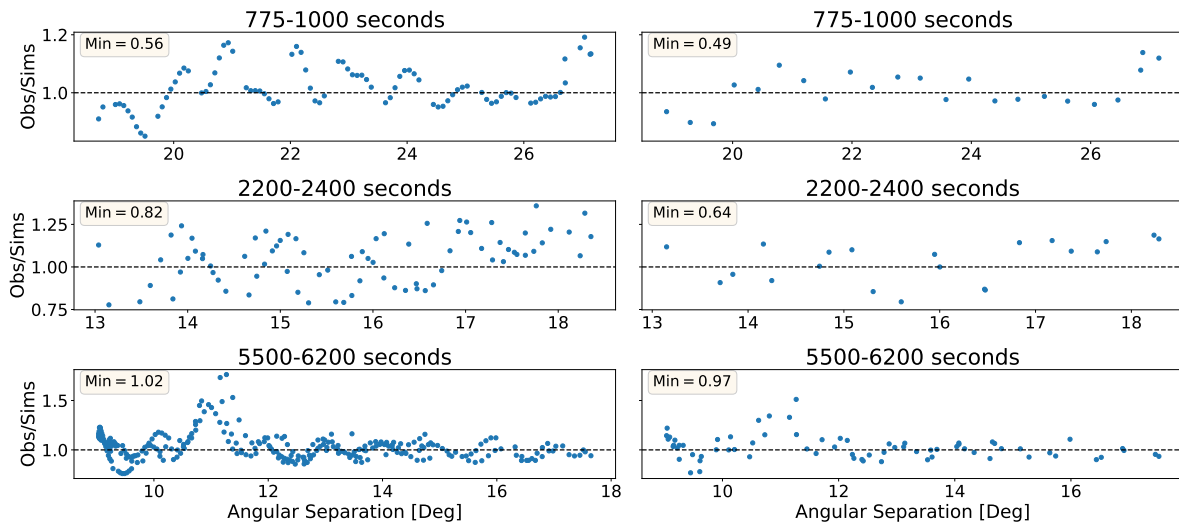


Figure 20. Ratio between the observational data and the model for the *temporal masking scenario*. Isolating a single Galileo satellite operating at a frequency range (averaged) of 1278.6-1278.8 MHz as it moves with respect to the MeerKAT pointing. The 1st, 2nd & 3rd rows represent the periods of 775-1000, 2200-2400 and 5500-6200 respectively. The left column is when no time average is applied, and the right is for a 10-second time average. The selected frequency is displayed with the CF for each panel.

and the satellite move, the same angular position of the satellite will be observed at different times. Therefore, we stack any time corresponding to the same angular position of the target satellite to increase the signal to noise. The panels on the left reveal a ringing effect that oscillates around one, essentially following the shape of the telescope primary beam. The obvious implication is that there is an error in the angular position which translates to an error in the beam value we should use. There could also be smaller contributions from other satellites since we cannot fully isolate the signal. Those would further mix up the ratio as they will be at different positions for the same times considered here.

Even in the far sidelobes, the beam can change significantly in relative terms, with ratios of up to 100 between the minimum and maximum values as the beam oscillates, with a period of about 1 degree. The dishes are moving in azimuth at speeds of 5 arcmin/s, e.g. they would move 10 arcmin within the time resolution of 2 sec, which can lead to a mismatch even if the satellite is not moving. We therefore consider smoothing both the data and simulation over 10 seconds. The idea is that any errors in the position as the dishes move back and forth could be averaged out. The results are shown in Figure 20. The oscillating structure seems to disappear, but part of that is simple because we now have fewer points. Overall, the ratio does get closer to 1, which improves the fitting, though not substantially.

In summary, the satellite central frequencies are well represented in the observational data. The frequency structure of the different Global signals in particular GPS, GAL and Beidou were well described even with the overlapping contribution from GAL and Beidou at 1268 MHz. One concern comes from the GLONASS whose emitted power and gain are not well sourced in literature. Another issue of GLONASS is that the 1248 MHz had several signals with similar frequency structures which can cause difficulty in the fit given the uncertainties in the tabulated specs. Apart from the GLONASS issue, the models appear to have a good representation of the data, as long as saturation is kept to a minimum. The other challenge is whether satellite signals weaken faster the further we are from the central frequency.

5 IMPACT ON THE COSMOLOGICAL BAND

So far, we have considered the impact of GNSS satellites around frequencies where they dominate. This allows for higher signal-to-noise when fitting the satellite simulations. These simulations can, in principle, be used to plan for observations that avoid strong contamination and also provide ways to flag the signal better. For cosmology, we have focused on a frequency band that we hope is completely free from satellite contamination, corresponding to 973-1015 MHz, where [Cunnington et al. \(2023a\)](#) presented a measurement of the cross-correlation power spectrum. To further help clean the data, the flagging algorithms will usually completely remove time stamps where the signal saturates, even if the contamination is low at the target frequencies. Figure 21 shows a comparison between the observation data and the simulation for two frequency channels within this "cosmology band". The same flags were applied to data and simulation, taken from [Wang et al. \(2021b\)](#). The α s in the simulation were first fitted using data from the frequencies where we clearly see satellite peaks (1100 - 1350 MHz).

Furthermore, to remove any background contamination, we have subtracted the time average for each channel, so the signal will fluctuate around zero. There is no obvious pattern in the data, which seems noise-dominated, and most of the satellite signal predicted by the simulations is within that noise. This makes it hard to try to fit for any out-of-band contamination from the satellites. However, it might happen that when we combine many observations together and calculate the HI power spectrum, some out-of-band signals from the satellites will still contaminate the cosmological signal. Indeed, in [Cunnington et al. \(2023a\)](#), we needed 30 PCA modes to clean the signal and achieve a detection. It's not clear what are the main reasons for such contamination. Probably a big part is related to issues in the bandpass calibration or other RFI. But it could be that there is some residual satellite contamination, although we do not see any obvious signature in the data. So in the next section, we use the fitted simulations to predict how much satellite contamination is expected in the cosmology band. We note that there is a fair

amount of uncertainty in the out-of-band emission due to the lack of information in the literature.

5.1 Extracting the HI power spectrum in the presence of satellites

Our goal in this section is to test the impact of satellites on the ability of MeerKAT to measure the HI power spectrum. To achieve this, we will combine the satellite simulations with simulations of the HI signal and foregrounds. This will then be processed in the same way as we would do for the data, with foreground cleaning followed by a power spectrum estimator. The procedure is similar to what is described in [Irfan et al. \(2024\)](#) where we go from time ordered data to data cubes and then power spectrum. To make the conclusions clearer we will neglect instrumental noise as this would tend to dilute any residual systematics.

We start by applying the same methodology as shown above to four more observational blocks. The inclusion of additional blocks (see [Table 1](#)) is to improve the sky coverage and include a good mix of satellites that are expected to show up on different days. We fitted the simulation to each block and tried different masking scenarios. In [Figure 22](#) we showcase three blocks (2 new additional blocks) using the best performing *full thermal masking scenario* with a thermal threshold of 33% of the maximum temperature to remove any saturated points. We decided to use these best fit models for further processing. The full simulated data blocks were then flagged. At this stage we opted to remove any data points with satellites closer than 5° . However, one of the blocks contains a GNSS satellite in geostationary orbit that is often below the 5° and would cause a large percentage of data to be masked. For this block, we applied a 1° flag instead. Since satellite movement differs across observations, the masks of the blocks do not overlap, and there are no gaps in the combined maps.

For the HI simulation, we used Gaussian density fields generated from a CMB power spectrum ([Lewis & Bridle 2002](#)) and generate HI maps at the sky positions we are observing. The Galactic emission component was generated assuming that the dominant contribution is from synchrotron emission and that synchrotron emission follows a power law parameterization:

$$T_{\text{sync}}(\nu, p) = T_{\text{amp}}(\nu, p) \left(\frac{\nu}{408} \right)^{\beta_{\text{sy}}(p)}, \quad (12)$$

where the amplitude template ($T_{\text{amp}}(\nu, p)$) at 408 MHz is the reprocessed, destriped Haslam 408 MHz map ([Remazeilles et al. 2015](#)) with the combined CMB monopole and unresolved point source background constant offset removed ([Wehus et al. 2017](#)). The spectral index template ($\beta_{\text{sy}}(p)$) is the model for the spectral index map from [Miville-Deschênes et al. \(2008\)](#).

Both the HI and Galactic foreground model required smoothing by the beam; whilst the EMSS beam is the optimal choice for modelling the satellite contributions, which are still of considerable magnitude up to several degrees away from the main lobe, a simple Gaussian beam model will suffice for smoothing the Galactic and HI contributions as the aim of these simulations was to assess the impact of the satellite residuals on top of a smoothed sky signal ([Matshawule et al. 2020](#)). The frequency-dependant Gaussian beam FWHM used was:

$$\theta_{\text{FWHM}}(\nu) = 1.2^\circ \times \frac{1280 \text{ MHz}}{\nu}. \quad (13)$$

Finally, following again [Irfan et al. \(2024\)](#), we use the RA and DEC information from each data block to extract the corresponding foreground and HI signal from the HEALPix ([Górski et al. 2005](#))

maps using tools from the `healpy` library. This way we generate equivalent TODs for the galactic synchrotron and HI.

For the five observation blocks, the residual satellite contributions are not visible by eye above the Galactic contributions within the TOD. [Figure 23](#) gives an example of this by showing the frequency-averaged TOD for block 1551055211, both with and without the satellite contribution included in the simulation.

We now have 5 observation blocks (time ordered data), each including satellite signal, HI and galactic synchrotron, convolved by the appropriate beam. As mentioned above, we do not include thermal noise so that we can test the results in the optimal case of high signal to noise, when small systematic residuals will become visible. A few ingredients are still missing: the receiver temperature, the elevation dependant temperature (ground pickup and atmosphere) and the CMB monopole. However, these are constant or fairly constant over the 90 minutes blocks. Since we actually remove a smooth function of time in the processing of the real data, we can just neglect these contributions here. This means that we have also removed the time average of the combined signal at each frequency for each of the 5 blocks time ordered data.

The five observation blocks are then combined at each frequency to make a 2D map in RA and DEC. The TOD samples (Y) are averaged into map pixels (X) using a pointing matrix (A):

$$X = (\mathbf{A}^T \mathbf{A})^{-1} \mathbf{A}^T Y, \quad (14)$$

which is assembled using the `astropy` coordinate library and setting the pixel spacing to be 0.4° (roughly two pixels per beam). Then, combining all the frequency maps, we have a 3D data cube. [Figure 24](#) shows the total system temperature map at frequency 983.5 MHz.

As the Galactic emission contribution dwarfs the HI signal, the maps require foreground cleaning before power spectra can be made. We aim to determine how residual satellite contamination corrupts a measurement of the HI signal in addition to standard problems of foreground cleaning, i.e. residual foreground contamination or conversely over-cleaning and removal of HI signal ([Cunnington et al. 2023b](#)). Therefore, we apply the same principal component analysis (PCA) foreground cleaning technique used in [Cunnington et al. \(2023a\)](#). We first calculated the frequency-frequency covariance matrix of our data cube, then removed the largest eigenvalues under the assumption that the signal with the strongest frequency correlation is the Galactic signal. We increased the number of modes removed until it was clear we had strong signal loss.

In order to better understand the residual contamination, we used an estimator based on the cross-correlation between the PCA-cleaned total emission maps and the input HI maps (as convolved with our Gaussian beam model). The cross-correlation power spectra were calculated using functionality from the HI simulations package `FastBox`¹⁴, which creates a 3D Cartesian data cube. In reality, future data will require a more robust regridding of the maps ([Cunnington & Wolz 2024](#)). The power was averaged between 9 bins in k -space spanning from $k = 0.02$ to $k = 0.7$. Twenty realisations of the HI signal were made so that we can calculate the mean and standard deviation of the mean for the estimators.

[Figure 25](#) shows the percentage deviation of the cross-correlation power spectra with respect to the HI signal, calculated as:

$$\frac{\Delta P(k)}{P_{\text{HI}}(k)} = \frac{\text{cross(cleaned)}}{\text{auto(HI)}} - 1 \quad (15)$$

¹⁴ <https://github.com/philbull/FastBox>

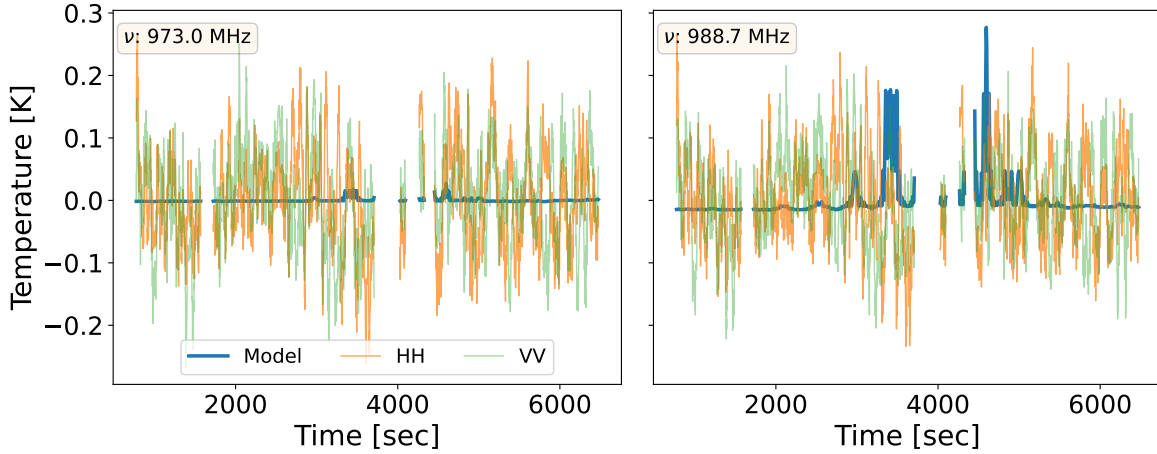


Figure 21. A temperature comparison across the observational scanning period between the satellite model (blue) and the residual calibrated observational data (W21) in the HH (orange) and VV (green) polarisation for the m000 antenna. Masks from W21 were included. The time average per channel is subtracted from each frequency channel. The frequency channels, 973.0 MHz (left panel) and 988.7 MHz (right panel), are selected as they reside in the cosmological band (973-1015 MHz) of the observation.

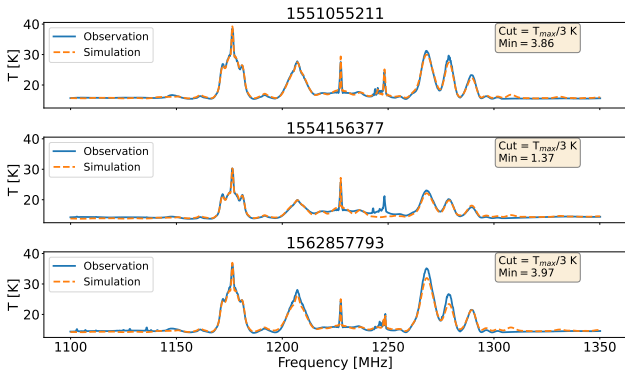


Figure 22. Best fit results for the *full thermal masking scenario* with a threshold (T_{Th}) = 33.33% and three observation blocks.

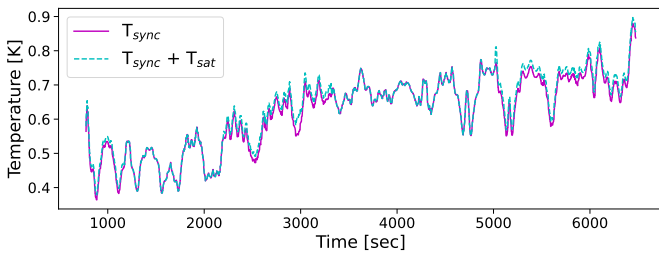


Figure 23. A comparison between the synchrotron emission only (magenta solid line) and the combined satellite and synchrotron emission (cyan dashed line) for the observational block of 155105211 after a 5° angular cut is applied.)

We considered two scenarios: the first where the only contaminant to the H_I signal is from diffuse Galactic synchrotron emission and the second where the contaminants are the combined Galactic and residual satellite temperatures. It can be seen that the removal of a single mode of frequency-correlated contaminants is enough for the scenario where only H_I and synchrotron emission are present in the

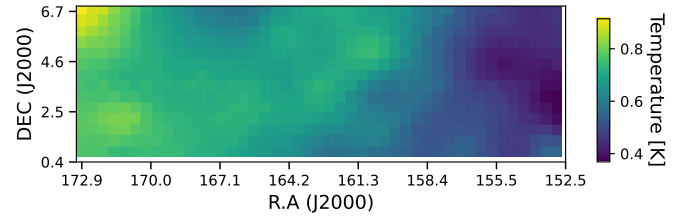


Figure 24. The combined system temperature map at $\nu = 983.5$ MHz for the five observation blocks. A pixel spacing of 0.4° was applied.

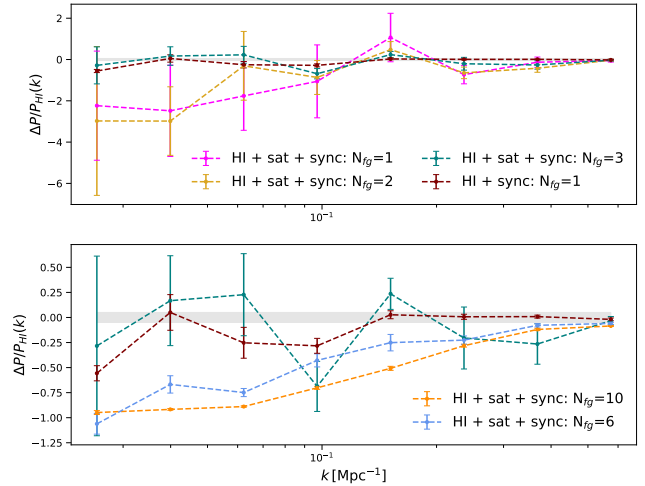


Figure 25. The percentage difference between our estimator and the H_I power spectrum. The estimator consists of the PCA cleaned cross-correlation power spectrum with the H_I signal itself and is a proxy for cross-correlations with galaxy surveys. The maroon curve represents H_I with synchrotron emission as the only contaminant and one PCA mode removed. The remaining curves contain residual satellite contamination with one (fuchsia), two (gold), 3 (teal), 6 (pastel blue) and 10 (orange) modes removed. The bottom panel highlights a zoomed-in version of the top panel with a larger number of modes removed.

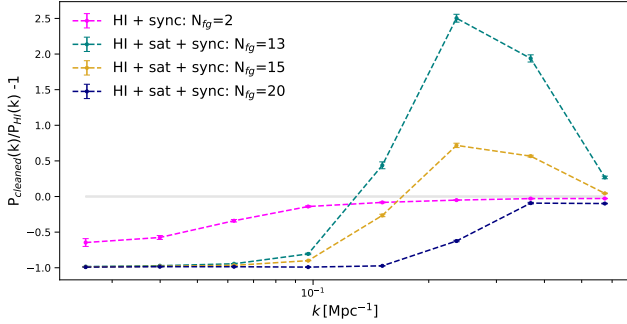


Figure 26. The auto-correlation for the HI power spectrum with different modes cleaned with PCA. The fuchsia curve represents HI with synchrotron emission as the only contaminant and two modes removed. Meanwhile, the remaining curves contain residual satellite contamination with 13 (teal), 15 (gold), and 20 (navy blue) modes removed. The grey straight line is the ratio for the HI only.

maps. For the inclusion of residual satellite emission, we show the effect of different numbers of modes removed, choosing to zoom in on the most significant number of modes removed (bottom panel) due to the scales of the y-axis.

We know that the satellite contamination is not smooth in frequency, so we do not necessarily expect PCA cleaning to work. Still, the power is reduced as we increase (slightly) the number of modes, showing that the PCA is able to distinguish the satellite signal from HI up to a certain point. At the largest k -scales, the residual satellite emission always adds power regardless of the level of cleaning, although increasing the number of modes decreases power. Conversely, at the smaller k -scales, the HI emission is dominant, and so all the power spectra start to converge to zero. We highlight the line of $\Delta P(k)/P_{HI}(k) = 0$ across all k -scales in grey as a visual aide.

Between the largest and smallest scales, the residual satellite contamination can be seen to cause fluctuations in power, which seems to imply a level of mode mixing between the residual satellite contamination, residual foreground contamination and the HI signal. Looking at the cross-power spectra for one mode removed compared to 10 modes removed, it can be seen that the level of mode mixing is inversely proportional to the number of modes removed, i.e: the more residual satellite contamination cleaned, the smoother the power spectrum ratio.

Although removing ten modes from the total emission maps results in the smoothest cross-correlation, we have over-cleaned to such an extent that the HI cannot be detected until $k > 0.3 \text{ Mpc}^{-1}$. Therefore we would argue that the optimum number of modes removed is three as this preserves HI, albeit slightly contaminated, across the largest number of k scales. We note that these results are based on the assumption that our simulations can be extended to these frequencies since no clear satellite signal is seen in this "cosmology" frequency band. Moreover, due to the intermittent nature of the satellite contamination, we expect this RFI contamination to average down as more blocks are combined.

Finally, we also consider looking at the HI in the autocorrelation (see Figure 26), which required a larger number of modes to be removed. With 20 modes removed, we could detect HI in the auto at the two largest k values but with strong signal loss across larger scales. Note as well that any robust conclusion on the number of modes removed requires an estimation of the signal loss, which is beyond the scope of this work.

6 CONCLUSION

The ability to determine the effects of RFI from satellite emissions has been and will continue to be a growing concern as more satellites enter Earth's orbit and the sensitivity of radio telescopes increase. Until now, flagging has been the primary tool by radio astronomers to deal with unwanted RFI from both terrestrial and orbital sources. However, even with removing contaminated channels, we fear emissions from these sources would progress into channels that we assumed to be clean. To investigate these effects, we developed in this paper a set of detailed simulations capable of predicting the signal of GNSS satellites across the sky and fitted these to real data from MeerKAT single dish observations. Note that while we have not gone into detail concerning other telecommunication satellites, particularly those in a geostationary orbit, we have looked at the possible impact these satellites have on our data. In appendix C, we outlaid the movement of two satellites that operate in the L-band. However, we saw no changes in the data that would correspond to the nearby movement of the satellites. This reaffirms ITU regulations that this L-sub-band is restricted to RNSS only.

We constructed a method to calibrate the usually flagged satellite emission within the 1140-1310 MHz region and applied it to data from the MeerKAT single-dish HI Intensity Mapping project (W21). We allowed the power of the different satellite signals to vary in the simulation and fitted their amplitude to the data. This is done for all frequencies and time-stamps. We found that the fitting starts failing when the signal becomes too strong, which we attribute to the system going non-linear (possibly from the Analog-to-Digital Converter). This usually occurs when a satellite operating in the frequency range of interest breaches the 5° angular separation distance from the telescope's pointing. To remedy this, we applied various masking scenarios ("angular", "thermal" and "full-thermal"). A 5° cut seems to perform well but leads to a high percentage of flagging. We found that masking all the time stamps when the signal goes above a certain threshold performs as well or better while keeping more data. We also see some temporal variation of the fitted signal power. This is probably not due to a true time dependence of the power but because of other uncertainties that are absorbed by our fitted amplitudes. In particular the fact that satellites in a constellation may have different signals while we assume they all share the same signals. Nevertheless, our fitted simulations are able to capture most of the structures seen in the data.

Finally, we looked at the effects of the satellite emission propagating to the lower frequency channels, mainly the 973-1015 MHz "Cosmology" frequency range. We showed that the simulated satellite signal is well within the observational data uncertainties for any given time dump and channel. The next step was to examine how satellite emission would affect the auto & cross-correlation of HI power spectrum at this frequency range. To check this, we ran end-to-end simulations for a few observational blocks that included HI and foregrounds. We saw that the satellite signal strongly contaminates the HI power spectrum. Applying PCA cleaning, we were able to recover the power spectrum reasonably well in cross-correlation, when removing more than 3 modes. The auto-power spectrum however, was strongly contaminated, requiring up to 20 modes and leading to strong signal loss. This may indicate that satellite contamination might be the dominant contaminant in our current L-band analysis, although such conclusion requires some extrapolation in our knowledge of the satellite out-of-band emission.

ACKNOWLEDGEMENTS

We thank Chris Finlay for useful discussions throughout the work and Wenkai Hu for comments on the draft. BNE and MGS acknowledge support from the South African Radio Astronomy Observatory and National Research Foundation (Grant No. 84156). We acknowledge using the ILIFU¹⁵ cloud computing facility through the Inter-University Institute for Data Intensive Astronomy. The South African Radio Astronomy Observatory, a facility of the National Research Foundation, an agency of the Department of Science and Innovation, operates the MeerKAT telescope. JF thanks the support of Fundação para a Ciência e a Tecnologia (FCT) through the research grants UIDB/04434/2020 and UIDP/04434/2020 and through the Investigador FCT Contract No. 2020.02633.CEECIND/CP1631/CT0002. This result is part of a project that has received funding from the European Research Council (ERC) under the European Union’s Horizon 2020 research and innovation programme (Grant agreement No. 948764). SC is supported by a UK Research and Innovation Future Leaders Fellowship grant [MR/V026437/1]. IPC is supported by the European Union within the Next Generation EU programme [PNRR-4-2-1.2 project No. SOE_0000136]. AP is a UK Research and Innovation Future Leaders Fellow [grant MR/X005399/1]. LW is a UK Research and Innovation Future Leaders Fellow [grant MR/V026437/1].

REFERENCES

Asad K. M. B., et al., 2021, *Monthly Notices of the Royal Astronomical Society*, **502**, 2970

Baan W., 2010, in RFI Mitigation Workshop. p. 1, doi:10.22323/1.107.0001

Baan W. A., 2019, *Journal of Astronomical Instrumentation*, **8**, 1940010

Battye R. A., Browne I. W. A., Dickinson C., Heron G., Maffei B., Pourtsidou A., 2013, *Monthly Notices of the Royal Astronomical Society*, **434**, 1239

Bentum M., Boonstra A. J., Baan W., 2010, in RFI Mitigation Workshop. p. 9, doi:10.22323/1.107.0009

Bharadwaj S., Nath B. B., Sethi S. K., 2001, *Journal of Astrophysics and Astronomy*, **22**, 21

Bigot-Sazy M. A., et al., 2016, in Qain L., Li D., eds, *Astronomical Society of the Pacific Conference Series Vol. 502, Frontiers in Radio Astronomy and FAST Early Sciences Symposium 2015*. p. 41 (arXiv:1511.03006), doi:10.48550/arXiv.1511.03006

Buch K. D., Kale R., Muley M., Kudale S., Ajithkumar B., 2023, *Journal of Astrophysics and Astronomy*, **44**, 37

Bull P., Ferreira P. G., Patel P., Santos M. G., 2015, *The Astrophysical Journal*, **803**, 21

Chang T.-C., Pen U.-L., Peterson J. B., McDonald P., 2008, *Phys. Rev. Lett.*, **100**, 091303

Chang T.-C., Pen U.-L., Bandura K., Peterson J. B., 2010, arXiv e-prints, p. arXiv:1007.3709

Cunnington S., Wolz L., 2024, *Monthly Notices of the Royal Astronomical Society*, **528**, 5586

Cunnington S., et al., 2023a, *Monthly Notices of the Royal Astronomical Society*, **518**, 6262

Cunnington S., et al., 2023b, *Monthly Notices of the Royal Astronomical Society*, **523**, 2453

Duffett-Smith P., Zwart J., 2017, *Coordinate Systems*. Cambridge University Press, p. 66–66

Finlay C., Bassett B. A., Kunz M., Oozeer N., 2023, *Monthly Notices of the Royal Astronomical Society*, **524**, 3231

Górski K. M., Hivon E., Banday A. J., Wandelt B. D., Hansen F. K., Reinecke M., Bartelmann M., 2005, *The Astrophysical Journal*, **622**, 759

Harper S. E., Dickinson C., 2018, *Monthly Notices of the Royal Astronomical Society*, **479**, 2024

Hobbs G., et al., 2020, *Publications of the Astronomical Society of Australia*, **37**

ITU I. T. U., 2004, List of ITU-R Recommendations and Reports, https://www.itu.int/dms_pub/itu-r/opb/rec/R-REC-LS-2004-PDF-E.pdf

ITU I. T. U., 2015, Recommendation ITU-R SM.1541-6

ITU I. T. U., 2021, Report ITU-R RA.2259-1

Irfan M. O., Li Y., Santos M. G., Bull P., Gu J., Cunnington S., Grainge K., Wang J., 2024, *Monthly Notices of the Royal Astronomical Society*, **527**, 4717

Lewis A., Bridle S., 2002, *Phys. Rev. D*, **66**, 103511

Masui K. W., et al., 2013, *The Astrophysical Journal*, **763**, L20

Matshawule S. D., Spinelli M., Santos M. G., Ngobese S., 2020, arXiv e-prints, p. arXiv:2011.10815

Mauch T., et al., 2020, *The Astrophysical Journal*, **888**, 61

Miville-Deschênes M.-A., Ysard N., Lavabre A., Ponthieu N., Macías-Pérez J. F., Aumont J., Bernard J. P., 2008, *Astronomy & Astrophysics*, **490**, 1093

Offringa A. R., et al., 2012, *Astronomy & Astrophysics*, **549**, A11

Remazeilles M., Dickinson C., Banday A. J., Bigot-Sazy M. A., Ghosh T., 2015, *Monthly Notices of the Royal Astronomical Society*, **451**, 4311

Rhodes B., 2019, Skyfield: High precision research-grade positions for planets and Earth satellites generator (ascl:1907.024)

Santos M., et al., 2015, in *Advancing Astrophysics with the Square Kilometre Array (AASKA14)*. p. 19 (arXiv:1501.03989)

Santos M. G., et al., 2017, arXiv e-prints, p. arXiv:1709.06099

Sihlangu I., Oozeer N., Bassett B. A., 2020, arXiv e-prints, p. arXiv:2008.08877

Teunissen P., Montenbruck O., 2017a, 4.3 Modulation Schemes. Springer International Publishing, p. 107–113

Teunissen P., Montenbruck O., 2017b, Annex B: GNSS Parameters. Springer International Publishing, p. 1235–1238

Wang Y., et al., 2021a, *Research in Astronomy and Astrophysics*, **21**, 018

Wang J., et al., 2021b, *Monthly Notices of the Royal Astronomical Society*, **505**, 3698

Wehus I. K., et al., 2017, *Astronomy & Astrophysics*, **597**, A131

de Villiers M. S., 2023, *AJ*, **165**, 78

APPENDIX A: GNSS POWER SPECTRUM DENSITY

Below are various binary offset carriers (BOC) used in this paper. We have incorporated them into our GNSS simulation and examples of their spectral shape we shown in subsection 2.3. These are a combination of sine and cosine sub-carriers. Here the sub-carrier rate is denoted as n_s . A value n is defined as $n = 2n_s/n_c$, which defines the number of half periods of the sub-carrier in one chip interval duration, where n_c is denoted as the chip rate. We denote the sine and cosine sub-carrier for the BOC as BOC_{\sin} and BOC_{\cos} , respectively. For simplicity we will set $w_c = \pi/n_c f_0$ and $w_s = \pi/n_s f_0$. f_0 is the reference frequency of the signal and is set at 1.023 MHz to obtain the spectrum $S_{xx} = |P_{xx}|^2$ where xx denotes the specific modulation in operation.

- BPSK:

$$P_{\text{BPSK}(n_c)}(\nu) = \frac{\text{sinc}(\pi\nu/[n_c f_0])}{\sqrt{n_c f_0}}. \quad (\text{A1})$$

- BOC_{\sin} & n even:

$$P_{\text{BOC}(n_s, n_c)}(\nu) = \sqrt{n_c f_0} \frac{\sin(w_c \nu)}{\pi \nu} \tan\left(\frac{w_s \nu}{2}\right) \quad (\text{A2})$$

¹⁵ www.life.ac.za

- BOC_{sin} & n odd:

$$P_{\text{BOC}(n_s, n_c)}(\nu) = \sqrt{n_c f_0} \frac{\cos(w_c \nu)}{\pi \nu} \tan\left(\frac{w_s \nu}{2}\right) \quad (\text{A3})$$

- BOC_{cos} & n even:

$$P_{\text{BOC}(n_s, n_c)}(\nu) = \sqrt{n_c f_0} \frac{\sin(w_c \nu)}{\pi \nu} \frac{1 - \cos\left(\frac{w_s \nu}{2}\right)}{\cos\left(\frac{w_s \nu}{2}\right)} \quad (\text{A4})$$

- BOC_{cos} & n odd:

$$P_{\text{BOC}(n_s, n_c)}(\nu) = \sqrt{n_c f_0} \frac{\cos(w_c \nu)}{\pi \nu} \frac{1 - \cos\left(\frac{w_s \nu}{2}\right)}{\cos\left(\frac{w_s \nu}{2}\right)} \quad (\text{A5})$$

- altBOC & n even ¹⁶:

$$S_{\text{alt}(n_s, n_c)}(\nu) = \frac{4n_c f_0}{\pi^2} \frac{\sin^2(w_c \nu)}{\cos^2\left(\frac{w_s \nu}{2}\right)} \phi_{n_s, n_c}(\nu) \quad (\text{A6})$$

- altBOC & n odd:

$$S_{\text{alt}(n_s, n_c)}(\nu) = \frac{4n_c f_0}{\pi^2} \frac{\cos^2(w_c \nu)}{\cos^2\left(\frac{w_s \nu}{2}\right)} \phi_{n_s, n_c}(\nu) \quad (\text{A7})$$

with

$$\phi_{n_s, n_c}(\nu) = \left[\cos^2\left(\frac{w_s \nu}{2}\right) - \cos\left(\frac{w_s \nu}{2}\right) - 2\cos\left(\frac{w_s \nu}{2}\right)\cos\left(\frac{w_s \nu}{4}\right) + 2 \right]$$

- TMBOC

Note that Composite BOC (CBOC)¹⁷ has the same modulation structure as TMBOC.

$$S_{\text{TMBOC}(6,1,1/11)}(\nu) = \frac{10}{11} S_{\text{BOCsin}(1,1)}(\nu) + \frac{1}{11} S_{\text{BOCsin}(6,1)}(\nu) \quad (\text{A8})$$

$$= \frac{f_0}{11\pi^2 \nu^2} \sin^2\left(\frac{\pi \nu}{f_0}\right) \left[10 \tan^2\left(\frac{\pi \nu}{2f_0}\right) + \tan^2\left(\frac{\pi \nu}{1f_0}\right) \right] \quad (\text{A9})$$

APPENDIX B: GNSS SIGNAL INFORMATION

Table B1 shows the number of satellites above the horizon for the telescope during the observation. In Table B2, we summarise the details we used to model the observed emission of the satellite constellation's signals.

APPENDIX C: GEOSTATIONARY SATELLITES

Besides the navigational satellites, many other satellites reside in a geostationary orbit around the Earth. These satellites generally operate at higher frequencies (K, KU, Ka-band) than their navigational

Const. #	GPS	GLO	GAL	BEI	IRNSS	SBAS	QZS
	15	13	13	18	5	9	0

Table B1. Number of satellites per constellation included, based on MeerKAT's field of view during the scanning period, for the observation on 25/02/2019 - 00:40:11 GMT.

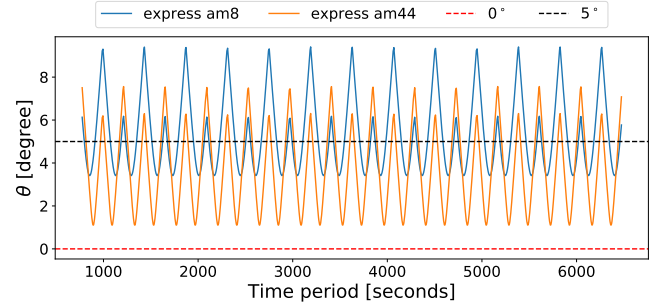


Figure C1. The angular distance (Equation 1) of two Russian geostationary communication satellites that transmit in the L-band and cross below the 5° boundary.

counterparts and belong to not only government agencies but private companies such as Starlink¹⁸ OneWeb¹⁹, etc... for communication purposes.

In our constructed satellite catalog, we excluded the telecommunication geostationary satellites due to the many unknown variables associated with them, in particular, their modulation and signal behavior. However, we can still track and locate satellites that enter the primary beam's 5° boundary. In our analysis, we found 17 satellites passed into the 5°, of which two were actively transmitting in the L-band. We show their θ movement concerning MeerKAT's pointing in Figure C1.

With the additional positional information, we created a new mask targeting the timestamps $\leq 5^\circ$ and combined this mask with the already in use 5° mask of the Galileo and GLONASS satellites. The additional masking removed ~83% of the data, which is less overall than the temporal masking but ~56% more than that of the 5°. In the case of the FoM, we obtained a C_1 value of 30855.53 and a C_2 value of 0.54. This shows a factor of 3 improvements when compared to only the 5° case (see Table 2).

However, we suspect that these two geostationary satellites do not emit within our frequency range of interest (1100-1350 MHz) for two reasons. (1) According to regulations the International Telecommunication Union sets, our frequency range is reserved for navigational satellite emission. (2) When comparing Figure C1 with the bottom panel of Figure 14 and Figure 17, it seems that the model can account for all the peaks of emission and overlay and accurate fit. This implies that there is no need to include extra satellite emission in the model.

This paper has been typeset from a $\text{\TeX}/\text{\LaTeX}$ file prepared by the author.

¹⁶ https://gssc.esa.int/navipedia/index.php/AltBOC_Modulation

¹⁷ <https://www.unoosa.org/documents/pdf/icg/activities/2007/icg2/presentations/24.pdf>

¹⁸ <https://www.starlink.com/>

¹⁹ <https://oneweb.net/>

#	Sys	Band	Signal	Frequency [MHz]	Modulation	Rate [MHz]	P_t [dBW]	G_t [dBi]
-	GPS	L1	P(Y)	1575.420	BPSK(10)	10.2300	13.5	13.5
-	GPS	L1	C/A	1575.420	BPSK(1)	1.0230	16.5	13.5
-	GPS	L1	L1C-D	1575.420	TMBOC(6,1,4/33)	1.0230	10.0	10.0
-	GPS	L1	M-D	1575.420	$\text{BOC}_{\sin}(10,5)$	5.1150	18.2	13.5
1	GPS	L2	P(Y)	1227.600	BPSK(10)	10.2300	10.0	10.0
2	GPS	L2	L2CM	1227.600	BPSK(1)	0.5115	10.0	10.0
3	GPS	L2	M-D	1227.600	$\text{BOC}(10,5)_{\sin}$	5.1150	16.0	13.5
4	GPS	L5	L5I	1176.450	BPSK(10)	10.2300	18.0	18.0
	GLO	L1	L1SF(P)	1602.000	BPSK(5)	5.1100	10.0	10.0
5	GLO	L2	L2SF(P)	1245.100	BPSK(5)	5.1100	10.0	10.0
6	GLO	L2	L2OF(C/A)	1245.100	BPSK(0.5)	0.5110	10.0	10.0
7	GLO	L3	L3OC-D	1202.025	BPSK(10)	10.2300	10.0	10.0
8	GLO	L2	L2OC-D	1248.300	BPSK(1)	1.0230	13.0	12.0
9	GLO	L2	L2OC-P	1248.300	$\text{BOC}(1,1)$	0.5115	5.0	5.0
-	GAL	E1	OS-D(B)	1575.420	$\text{CBOC}(6,1,1/11)$	1.0230	10.0	10.0
10	GAL	E6	CS-P(C)	1278.750	BPSK(5)	5.1150	16.0	15.0
11	GAL	E6	PRS(A)	1278.750	$\text{BOC}_{\cos}(10,5)$	5.1150	18.0	16.0
12	GAL	E5ab	PRS(A)	1191.795	$\text{AltBOC}(15,10)$	10.2300	10.0	10.0
13	GAL	E5a	E5a-D	1176.450	$\text{AltBOC}(15,10)$	10.2300	6.0	6.0
-	BDS-2	B1-2	RS	1561.098	BPSK(2)	2.0460	10.0	10.0
14	BDS-2	B3	RS	1268.520	BPSK(10)	10.2300	16.0	16.0
15	BDS-2	B2b	OS	1207.140	BPSK(2)	2.0460	14.0	12.0
16	BDS-2	B2b	RS	1207.140	BPSK(10)	10.2300	18.0	18.0
-	BDS-3	B1-2	OS	1561.098	BPSK(2)	2.0460	10.0	10.0
-	BDS-3	B1	B1C-DI	1575.420	TMBOC(6,1,4/33)	1.0230	10.0	10.0
17	BDS-3	B3	B3C-Dm	1268.520	BPSK(10)	10.2300	15.0	13.5
18	BDS-3	B3	B3A-Dm	1268.520	$\text{BOC}(15,2,5)$	2.5575	10.0	10.0
-	QZS-1	L1	C/A	1575.420	BPSK(1)	1.0230	10.0	10.0
-	QZS-1	L1	L1C-D	1575.420	$\text{BOC}(1,1)$	1.0230	10.0	10.0
-	QZS-1	L1	L1C-D	1575.420	TMBOC(6,1,4/33)	1.0230	10.0	10.0
-	QZS-1	L1	SAIF	1575.420	BPSK(1)	1.0230	10.0	10.0
-	QZS-1	L2	L2CL	1227.600	BPSK(1)	0.5115	10.0	10.0
-	QZS-1	L6	L61(LEX) _n	1278.750	BPSK(5)	5.1150	10.0	10.0
-	QZS-1	L6	L62o	1278.750	BPSK(5)	5.1150	10.0	10.0
-	QZS-1	L5	L5I	1176.450	BPSK(10)	10.2300	16.0	16.0
-	QZS-1	L5	L5Q	1176.450	BPSK(10)	10.2300	16.0	16.0
19	IRNSS	L5	SPS	1176.450	BPSK(1)	1.0230	16.0	14.0
20	IRNSS	L5	RS-D	1176.450	$\text{BOC}(5,2)$	2.0460	18.0	16.0
-	SBAS	L1	C/A	1575.420	BPSK(1)	1.0230	13.0	13.5
21	SBAS	L5	L5I	1176.450	BPSK(10)	10.2300	18.0	16.0

Table B2. List of satellite signals used in the simulation. Only signals with an index were potentially present and therefore included (first column). "Sys": constellation system; "Band": allocation of signal transmission; "Signal": name of radio transmission; "Frequency": peak frequency of transmission; "Modulation": frequency structure of signal; "Rate": $n_c \times f_0$; " P_t ": transmitted power of transmission; " G_t ": antenna gain of transmission (Harper & Dickinson 2018; Teunissen & Montenbruck 2017b). The highlighted grey regions indicate the signals we considered for each of the constellations. All the satellites from a given constellation are assumed to have the same signals.